

A new partially integrated transport model for subgrid-scale stresses and dissipation rate for turbulent developing flows

Bruno Chaouat

Department of Computational Fluid Dynamics, ONERA, 92322 Châtillon, France

Roland Schiestel

IRPHE, Château-Gombert, 13384 Marseille, France

(Received 21 July 2004; accepted 24 February 2005; published online 3 June 2005; publisher error corrected 11 July 2005)

A new subgrid-scale turbulence model involving all the transport equations of the subgrid-scale stresses and including a dissipation rate equation is proposed for large-eddy simulation (LES) of unsteady flows which present nonequilibrium turbulence spectra. Such a situation in flow physics occurs when unsteadiness is created by forced boundary conditions, but also in more complex situations, when natural unsteadiness develops due to the existence of organized eddies. This latter phenomenon explains the instability found in a porous-walled chamber with mass injection. Due to the high value of Reynolds number, the presence of wall boundaries, and the use of relatively coarse grids, the spectral cutoff may be located before the inertial zone of the energy spectrum. The use of transport equations for all the subgrid-scale stress components allows us to take into account more precisely the turbulent processes of production, transfer, pressure redistribution effects, and dissipation, and the concept of turbulent viscosity is no longer necessary. Moreover, some backscatter effects can possibly arise. As a result of modeling in the spectral space, a formally continuous derivation of the model is obtained when the cutoff location is varied, which guarantees compatibility with the two extreme limits that are the full statistical Reynolds stress transport model of Launder and Shima and direct numerical simulation. In the present approach, due to the presence of the subgrid-scale pressure-strain correlation term in the stress equations, the new subgrid model is able to account for history and nonlocal effects of the turbulence interactions, and also to describe more accurately the anisotropy of the turbulence field. The present model is first calibrated on the well-known fully turbulent channel flow. For this test case, the LES simulation reveals that the computed velocities and Reynolds stresses agree very well with the DNS data. The application to the channel flow with wall mass injection which undergoes a transition process from laminar to turbulent regime and the development of natural unsteadiness is then considered for illustrating the potentials of the method. LES results are compared with experimental data including the velocity components, the turbulent stresses, and the transition location. A satisfactory agreement is obtained for both the mean quantities and the turbulent field. In addition, structural information of the flow is provided. © 2005 American Institute of Physics. [DOI: 10.1063/1.1928607]

I. INTRODUCTION

Advanced statistical models based on the Reynolds averaged Navier–Stokes equations (RANS) such as the Reynolds stress model (RSM), described in detail by Speziale *et al.*,¹ can be able to accurately predict complex flows for engineering applications, as, for instance, flows with strong effects of streamline curvature, system rotation, or wall injection, as shown by Chaouat.^{2,3} However, these models based on one-point closure are not well suited for unsteady flows subjected to medium range frequencies that can interact with the turbulence scales. Furthermore, they cannot provide information on turbulence structures, two-point correlation statistics, or energy spectrum which can be useful for investigating the flow characteristics. Due to the progress in powerful computers, large-eddy simulation (LES) is a promising route toward the calculation of turbulent flows which has been now largely developed. This approach consists in modeling the more universal small scales, while the large-scale mo-

tions are explicitly calculated. It assumes that the filter cutoff occurs at a wave number which is located in the inertial range for equilibrium flows. LES thus appears to be a good compromise between direct numerical simulation (DNS) which resolves all the turbulent scales and RANS statistical modeling in which the whole flow structures are modeled. Contrary to full statistical modeling, LES enables us to mimic the mechanisms of turbulent interactions, and information on velocity or pressure fluctuations and on two-point correlations are possible. In the past, the most widely used subgrid-scale model was a viscosity type model proposed by Smagorinsky.⁴ It is based on an implicit equilibrium hypothesis which assumes that the viscosity can be calculated using the resolved scales as a characteristic velocity and the grid size as a characteristic length. It was first applied to channel flows by Deardorff⁵ and more recently by Moin and Kim.⁶ Many flow studies can be found in the scientific literature that have used this model. However, it soon appeared that the

Smagorinsky constant is not universal and must be varied from one flow to another. As mentioned by Lesieur,⁷ new trends in LES of turbulence have been proposed in the past decade, such as, for instance, the dynamic model developed by Germano *et al.*⁸ or the structure model of Métais and Lesieur.⁹ Transport equations of the subgrid-scale turbulent kinetic energy with an algebraic relation for the length scale given by the mesh cell size have been proposed by Schumann,¹⁰ Horiuti and Yoshizawa,¹¹ and more recently by Dejoan and Schiestel.¹² Deardorff,¹³ was the first author to propose stress transport equations for subgrid-scale turbulence.

Despite improvements in the more advanced approaches, several modeling problems remain. For instance, the filter width may no longer be a good estimate of the characteristic subgrid-scale turbulence length when the filter cutoff is located at a wave number below the inertial range in nonequilibrium flows. To overcome this problem, Dejoan and Schiestel¹⁴ have developed a new LES model based on two transport equations for the subgrid-scale energy and the dissipation rate ϵ equation. In this approach, the transport equation for the dissipation rate is used for calculating the length scale without referring directly to the mesh size. Applications of partially integrated transport modeling (PITM) to unsteady turbulence submitted to periodic forcing in pulsed channel flow have illustrated the potentials of this method.¹⁵

The aim of the present study is to propose a new LES approach involving all the stress transport equations of the subgrid-scale turbulence including also the dissipation rate equation. The approach is based on the work of Dejoan and Schiestel¹⁴ which is extended to subgrid-scale Reynolds stresses components. This modeling strategy is motivated by the idea that the recognized advantages of usual second-order closures (RSM) are worth to be transposed to subgrid-scale (SGS) modeling when the SGS part is not small compared to the resolved part. In particular, due to the presence of the subgrid-scale pressure-strain correlation term in the transport equations, this new model embodies interesting features allowing a more realistic description of the flow anisotropy than eddy viscosity models, and also a better account of history and nonlocal effects.

In that type of LES approach, it is of importance to note that the model behavior must be dependent on the location of the cutoff imposed by the filter width. The model formulation will be built such that the new subgrid-scale model can vary continuously between the two extreme limits that are the direct numerical simulation (without any modeling) and the full statistical Reynolds stress model of Launder and Shima.¹⁶

This PITM approach seems particularly relevant for studying turbulent flows with nonstandard spectral distributions (with some departure from the standard Kolmogorov spectrum) and also relatively coarse grids. So, this approach enables us to bridge URANS and LES methods. Recently, this line of thought appeared to gain major interest in turbulence modeling not only from the fundamental and theoretical points of view but also for practical reasons as mentioned, for instance, by Germano¹⁷ and Spalart.¹⁸ The main applications will be concerned with simulations of turbulent

flows which undergo nonequilibrium changes such as produced by unsteadiness (forced or natural) in the mean or strong spatial variations on relatively coarse grids. In order to calibrate the present model, LES of fully turbulent channel flow is performed and the velocity and the Reynolds stresses components are compared with available DNS data of Moser *et al.*¹⁹ The application to the channel flow with wall injection is then considered for illustrating the potentials of the method. This case is of central interest for engineering applications in solid rocket motors (SRM). The mass transfer resulting from the propellant combustion produces an internal flowfield with different flow regimes, from laminar to turbulent, which affects the ballistics predictions of the rocket, as observed by Chaouat and Schiestel.²⁰ In that framework of SRM applications, it is of interest to note that Wasistho and Moser²¹ have proposed recently a turbulence strategy based on a zonal modeling approach such as an interface between detached eddy simulation (DES) near the wall and LES away from the wall. In the present study, we show that the subgrid-scale model is able to reproduce a good description of the injection induced flow and the underlying acting mechanisms. Comparisons with existing experimental data are made for the velocity, the stresses, and the turbulent transition process.

II. GOVERNING EQUATIONS

We consider the turbulent flow of a viscous fluid. As in the usual treatment of turbulence, the flow variable ξ is decomposed into a filtered part including mean value and large-scale fluctuation $\bar{\xi}$ and a subgrid-scale fluctuating part ξ' such as

$$\xi = \bar{\xi} + \xi', \quad (1)$$

the quantity $\bar{\xi}$ is defined by the filter function G_Δ as

$$\bar{\xi} = \int \prod_{i=1}^3 G_{\Delta_i}(x_i, x'_i) \xi(x'_1, x'_2, x'_3) dx'_1 dx'_2 dx'_3, \quad (2)$$

where Δ_i is the filter width in the i th direction. The Reynolds statistical average of ξ is denoted by $\langle \xi \rangle$ so that the large scale fluctuation is $\bar{\xi} - \langle \xi \rangle$. In the present case, the Favre averaging²² is used for compressible flows. In that definition, the variable ξ can be written as

$$\xi = \tilde{\xi} + \xi'' \quad (3)$$

leading to $\tilde{\xi} = \bar{\rho} \bar{\xi} / \bar{\rho}$. The filtered equations of the mass, the momentum, and the energy are

$$\frac{\partial \bar{\rho}}{\partial t} + \frac{\partial}{\partial x_j} (\bar{\rho} \tilde{u}_j) = 0, \quad (4)$$

$$\frac{\partial}{\partial t} (\bar{\rho} \tilde{u}_i) + \frac{\partial}{\partial x_j} (\bar{\rho} \tilde{u}_i \tilde{u}_j) = \frac{\partial}{\partial x_j} (\bar{\sigma}_{ij} - \bar{\rho} \tilde{u}_i'' \tilde{u}_j''), \quad (5)$$

$$\frac{\partial}{\partial t}(\overline{\rho E}) + \frac{\partial}{\partial x_j}(\overline{\rho E \tilde{u}_j}) = \frac{\partial}{\partial x_j}(\overline{\sigma_{ij} \tilde{u}_i}) - \frac{\partial \bar{q}_i}{\partial x_j} + \frac{\partial}{\partial x_j}(\overline{\sigma_{ij} u_i'' - \rho E'' u_j''}), \quad (6)$$

where u_i , E , σ_{ij} , q_i are, respectively, the velocity vector, the total energy, the tensorial term composed by the pressure and the viscous tensor, and the total heat flux vector. In these expressions, the $\bar{\sigma}_{ij}$ tensor takes the form

$$\bar{\sigma}_{ij} = \bar{\mu} \left(\frac{\partial \bar{u}_i}{\partial x_j} + \frac{\partial \bar{u}_j}{\partial x_i} \right) - \left(\bar{p} \delta_{ij} + \frac{2}{3} \bar{\mu} \frac{\partial \bar{u}_k}{\partial x_k} \delta_{ij} \right), \quad (7)$$

where μ stands for the molecular viscosity. The subgrid-scale Reynolds stress tensor for the fluctuating velocities is

$$(\tau_{ij})_{\text{SGS}} = \widetilde{u_i'' u_j''}. \quad (8)$$

The filtered heat flux is computed using Fourier law,

$$\bar{q}_i = -\bar{\chi} \frac{\partial \bar{T}}{\partial x_i}, \quad (9)$$

where T is the temperature and χ stands for the thermal conductivity. Assuming ideal gas law, $p = \rho RT / \mathcal{M}$, where R is the universal gas constant and \mathcal{M} is the molecular weight; the filtered thermodynamic pressure is computed as

$$\bar{p} = (\gamma - 1) \bar{\rho} \left(\bar{E} - \frac{1}{2} \widetilde{u_i'' u_i''} - \frac{1}{2} \widetilde{u_i'' u_i''} \right). \quad (10)$$

The presence of a turbulent contribution $\widetilde{u_i'' u_i''}$ in Eq. (10) shows the usual coupling between the filtered equations and the turbulent transport equations. The fluctuating correlation which appears in the right-hand side in the energy equation (6) can be developed as

$$\overline{\sigma_{ij} u_i''} - \overline{\rho E'' u_j''} \approx \bar{\rho} \widetilde{u_i'' u_j''} + \bar{\rho} \widetilde{h'' u_j''}, \quad (11)$$

where h is the enthalpy of the fluid, so that the closure of the mean flow equations is necessary for the subgrid-scale turbulent stress $\bar{\rho} \widetilde{u_i'' u_j''}$ as well as for the turbulent heat flux $\widetilde{h'' u_j''}$.

III. SUBGRID-SCALE TURBULENCE MODEL USING TRANSPORT EQUATIONS

A. Modeling concept of the new approach

The exact filtered transport equation of the subgrid-scale stress tensor $u_i' u_j'$ takes the following form in incompressible fluid flow using Eq. (1) decomposition:²³

$$\frac{\partial}{\partial t}(\overline{\rho u_i' u_j'}) + \frac{\partial}{\partial x_k}(\overline{\rho u_i' u_j' u_k'}) = P_{ij} - \rho \epsilon_{ij} + \Phi_{ij} + J_{ij}, \quad (12)$$

with

$$P_{ij} = -\overline{\rho u_i' u_k' \frac{\partial u_j'}{\partial x_k}} - \overline{\rho u_j' u_k' \frac{\partial u_i'}{\partial x_k}},$$

$$\epsilon_{ij} = 2\nu \overline{\frac{\partial u_i'}{\partial x_k} \frac{\partial u_j'}{\partial x_k}},$$

$$\Phi_{ij} = \overline{p' \left(\frac{\partial u_i'}{\partial x_j} + \frac{\partial u_j'}{\partial x_i} \right)},$$

$$J_{ij} = -\rho \frac{\partial}{\partial x_k} \overline{u_i' u_j' u_k'} + \rho u_j' \frac{\partial}{\partial x_k} \overline{u_i' u_k'} + \rho u_i' \frac{\partial}{\partial x_k} \overline{u_j' u_k'} - \frac{\partial}{\partial x_i} \overline{p' u_j'} - \frac{\partial}{\partial x_j} \overline{p' u_i'} + \mu \frac{\partial^2 \overline{u_i' u_j'}}{\partial x_k \partial x_k}. \quad (13)$$

The terms on the right-hand side of Eq. (13) are identified as the production by the filtered velocity P_{ij} , the turbulent viscous dissipation ϵ_{ij} , the redistribution of the subgrid-scale turbulent kinetic energy among the stress components Φ_{ij} , and the diffusion caused by the fluctuating velocities J_{ij} together with the molecular diffusion.

The modeling of the filtered transport equation of the subgrid-scale stress tensor lies on the analysis of the turbulent processes in the spectral space. In this framework, a cutoff wave number κ_c is introduced in the medium range of eddies while the wave number κ_d is located at the end of the inertial range of the spectrum after the transfer zone. The subgrid-scale energy in the range $[\kappa_c, \kappa_d]$ is denoted as $k_{\text{SGS}} = (\tau_{mm})_{\text{SGS}} / 2$. We introduce the dimensionless wave number $\eta_c = \kappa_c k^{3/2} / \epsilon$ using the cutoff wave number κ_c and a macroturbulent length scale computed by means of k and ϵ , where k denotes the total turbulent kinetic energy (resolved part and modeled part).¹⁴

From Eq. (12), the turbulent transport equation of the subgrid-scale tensor $(\tau_{ij})_{\text{SGS}} = \widetilde{u_i'' u_j''}$ for compressible flows can be modeled as

$$\begin{aligned} \frac{\partial}{\partial t}[\bar{\rho}(\tau_{ij})_{\text{SGS}}] + \frac{\partial}{\partial x_k}[\bar{\rho}(\tau_{ij})_{\text{SGS}} \tilde{u}_k] \\ = P_{ij} - \bar{\rho} \epsilon_{ij} + \Phi_{ij}^1 + \Phi_{ij}^2 + \Phi_{ij}^w + J_{ij}, \end{aligned} \quad (14)$$

where

$$P_{ij} = -\bar{\rho}(\tau_{ik})_{\text{SGS}} \frac{\partial \tilde{u}_j}{\partial x_k} - \bar{\rho}(\tau_{jk})_{\text{SGS}} \frac{\partial \tilde{u}_i}{\partial x_k}, \quad (15)$$

$$\epsilon_{ij} = \frac{2}{3} \epsilon \delta_{ij}. \quad (16)$$

Although the density is variable, the fluctuating density is neglected in the present applications. The redistribution terms Φ_{ij}^1 , Φ_{ij}^2 , and Φ_{ij}^w of the pressure-strain subgrid-scale fluctuating correlations must be modeled. In the limit of vanishing η_c , the spectral cutoff goes to zero and the assumptions are chosen in order to recover the usual statistical model of Launder and Shima.¹⁶ In accordance with that condition, we propose the following model hypotheses in the range $[\kappa_c, \kappa_d]$:

$$\Phi_{ij}^1 = -c_{\text{SGS}1} \bar{\rho} \frac{\epsilon}{k_{\text{SGS}}} \left[(\tau_{ij})_{\text{SGS}} - \frac{2}{3} k_{\text{SGS}} \delta_{ij} \right], \quad (17)$$

$$\Phi_{ij}^2 = -c_2 (P_{ij} - \frac{1}{3} P_{mm} \delta_{ij}). \quad (18)$$

Equation (17) characterizes nonlinear interactions. Equation (18) represents the linear contribution of the return to isotropy with respect to the velocity gradients. According to the

TABLE I. Functions used in the subgrid-scale model.

c_1	$1 + 2.58AA_2^{1/4}(1 - \exp\{-(1/150)R_i\}^2)$
c_2	$3/4A^{1/2}$
c_1^w	$-2/3c_1 + 5/3$
c_2^w	$\max(2/3c_2 - 1/6, 0)/c_2$
f_w	$0.4k_{SGS}^{3/2}/\epsilon x_n$

classical physics of turbulence, the coefficient c_{SGS_1} must increase with the parameter η_c in order to increase the return to isotropy in the range of larger wave numbers. To do that, we suggest a simple empirical function

$$c_{SGS_1} = \frac{1 + \alpha_\eta \eta_c^2}{1 + \eta_c^2} c_1, \quad (19)$$

where α_η is a numerical constant. This function satisfies the limiting condition

$$\lim_{\eta_c \rightarrow 0} c_{SGS_1}(\eta_c) = c_1. \quad (20)$$

In this formulation, like in the Launder and Shima model, the function c_1 depends on the second and third subgrid-scale invariants $A_2 = a_{ij}a_{ji}$, $A_3 = a_{ij}a_{jk}a_{ki}$, and the flatness coefficient parameter $A = 1 - \frac{9}{8}(A_2 - A_3)$, where $a_{ij} = [(\tau_{ij})_{SGS} - \frac{2}{3}k_{SGS}\delta_{ij}]/k_{SGS}$. The term Φ_{ij}^w takes into account the wall reflection effect of the pressure fluctuations and is embedded in the model for reproducing correctly the logarithmic region of the turbulent boundary layer. It is modeled according to the previous work of Gibson:²⁴

$$\begin{aligned} \Phi_{ij}^w = c_1^w \frac{\bar{\rho}\epsilon}{k_{SGS}} & \left[(\tau_{kl})_{SGS} n_k n_l \delta_{ij} - \frac{3}{2} (\tau_{kl})_{SGS} n_k n_j \right. \\ & \left. - \frac{3}{2} (\tau_{kj})_{SGS} n_k n_i \right] f_w \\ & + c_2^w \left(\Phi_{kl}^2 n_k n_l \delta_{ij} - \frac{3}{2} \Phi_{ik}^2 n_k n_j - \frac{3}{2} \Phi_{jk}^2 n_k n_i \right) f_w, \end{aligned} \quad (21)$$

where n_i is the unit vector perpendicular to the wall surface and f_w is a near wall damping function. The diffusion process J_{ij} is modeled assuming a gradient law

$$J_{ij} = \frac{\partial}{\partial x_k} \left(\bar{\mu} \frac{\partial (\tau_{ij})_{SGS}}{\partial x_k} + c_s \bar{\rho} \frac{k_{SGS}}{\epsilon} (\tau_{kl})_{SGS} \frac{\partial (\tau_{ij})_{SGS}}{\partial x_l} \right), \quad (22)$$

where c_s is a numerical coefficient which takes the value 0.22. The functions used in that subgrid model are listed in Table I. Note that the transport equation of the subgrid-scale turbulent energy can be easily obtained from Eq. (14) by contracting the tensor $(\tau_{ij})_{SGS}$ over its indices:

$$\frac{\partial}{\partial t} (\bar{\rho} k_{SGS}) + \frac{\partial}{\partial x_m} (\bar{\rho} k_{SGS} \tilde{u}_m) = \frac{1}{2} P_{mm} - \bar{\rho}\epsilon + \frac{1}{2} J_{mm}. \quad (23)$$

In contrast to the two-equation model, it can be mentioned that the production term P_{ij} is allowed to become negative. In such a case, this implies that energy is transferred from the filtered motions up to the resolved motions, known as backscatter process.

The dissipation rate ϵ which appears in Eq. (16) is computed by means of a transport equation. As for the transport equation of the subgrid-scale velocity fluctuations, this equation is modeled by considering the turbulent processes which develop in the spectral space, or more precisely, in a spectral slice. This method has been applied in multiple-time-scale modeling of turbulent flows in one-point closures.²⁵ In a first step, the case of homogeneous anisotropic turbulence is considered. The constant value of the mean velocity gradient is denoted Λ_{ij} . The equation of the energy spectrum balance $E(\kappa)$ is obtained by taking the Fourier transform and mean value on spherical shells of the transport equation of the two-point velocity correlation:^{26,27}

$$\frac{\partial E}{\partial t} = -\Lambda_{ij} A_{ij} + T - 2\nu\kappa^2 E. \quad (24)$$

The three terms on the right-hand side of this equation represent the production caused by the mean velocity gradient, the spectral transfer which results from triad interactions of wave number modes, and the viscous dissipation.²⁸ The term A_{ij} corresponds to the spherical mean of the spectral tensor of the double velocity correlations in wave vector space. Integration of the basic equation (24) over the wave number range $[\kappa_{j-1}, \kappa_j]$ yields the following equation:

$$\frac{\partial k_{[\kappa_{j-1}, \kappa_j]}}{\partial t} = P_{[\kappa_{j-1}, \kappa_j]} - F(\kappa_j) + F(\kappa_{j-1}) - \epsilon_{[\kappa_{j-1}, \kappa_j]}, \quad (25)$$

with the relations

$$k_{[\kappa_{j-1}, \kappa_j]} = \int_{\kappa_{j-1}}^{\kappa_j} E(\kappa) d\kappa, \quad (26)$$

$$P_{[\kappa_{j-1}, \kappa_j]} = -\Lambda_{lm} \int_{\kappa_{j-1}}^{\kappa_j} A_{lm}(\kappa) d\kappa, \quad (27)$$

$$F(\kappa_j) = \mathcal{F}(\kappa_j) - E(\kappa_j) \frac{\partial \kappa_j}{\partial t}, \quad (28)$$

$$\mathcal{F}(\kappa) = \int_{\kappa}^{\infty} T(\kappa') d\kappa' = - \int_0^{\kappa} T(\kappa') d\kappa', \quad (29)$$

$$\epsilon_{[\kappa_{j-1}, \kappa_j]} = 2\nu \int_{\kappa_{j-1}}^{\kappa_j} \kappa^2 E(\kappa) d\kappa. \quad (30)$$

Here \mathcal{F} represents the spectral energy rate transferred into the wave number range $[\kappa, +\infty]$ by vortex stretching from the wave number range $[0, \kappa]$. Equation (25) can be applied for any wave number range such as $[0, \kappa_c]$, $[\kappa_c, \kappa_d]$, and $[\kappa_d, \infty[$. Taking into account the significant processes, one can obtain the following approximated equations:

$$\frac{\partial(k - k_{SGS})}{\partial t} = P_{[0, \kappa_c]} - F(\kappa_c), \quad (31)$$

$$\frac{\partial(k_{SGS})}{\partial t} = P_{[\kappa_c, \kappa_d]} - F(\kappa_d) + F(\kappa_c), \quad (32)$$

$$0 = F(\kappa_d) - \epsilon_{[\kappa_d, \infty[}, \quad (33)$$

where $\epsilon_{[\kappa_d, \infty[} \approx \epsilon$. Equation (33) indicates that the dissipation rate ϵ can indeed be interpreted as a spectral flux. Equation (32) is compared to Eq. (A6) which is developed in physical space (cf. the Appendix) and yields the exact expressions for the production, transfer, and dissipation rates

$$P_{[\kappa_c, \kappa_d]} = -\langle u'_i u'_j \rangle \frac{\partial \langle u_i \rangle}{\partial x_j}, \quad (34)$$

$$F(\kappa_c) = -\left\langle u'_i u'_j \frac{\partial v_i}{\partial x_j} \right\rangle, \quad (35)$$

$$\epsilon = \nu \left\langle \frac{\partial u'_i}{\partial x_j} \frac{\partial u'_i}{\partial x_j} \right\rangle. \quad (36)$$

In Eq. (35), $v_i = \bar{u}_i - \langle u_i \rangle$ denotes the large-scale fluctuating velocity component which is the difference between the filtered and the statistical mean velocity. Note that a term by term summation of Eqs. (31)–(33) provides the transport equation of the total turbulent kinetic energy k ,

$$\frac{\partial k}{\partial t} = P_{[0, \kappa_d]} - \epsilon, \quad (37)$$

where $P_{[0, \kappa_d]} \approx P_{[0, \infty[}$. In the present approach, the splitting wave number κ_d is assumed to be related to the cutoff wave number κ_c by the dimensional relation

$$\kappa_d - \kappa_c = \zeta_{\text{SGS}} \frac{\epsilon}{k_{\text{SGS}}^{3/2}}, \quad (38)$$

where ζ_{SGS} is a coefficient which may be dependent on the spectrum shape and on the Reynolds number. The relation (38) is proposed for adjusting the location of the cutoff wave number to the evolving spectrum. The dissipation rate equation is then obtained by taking the derivative of Eq. (38) with respect to time using Eq. (28) written for the wave number κ_d :

$$\frac{\partial \kappa_d}{\partial t} = \frac{\mathcal{F}(\kappa_d) - F(\kappa_d)}{E(\kappa_d)}. \quad (39)$$

Taking into account (32) and (33), one can easily obtain

$$\frac{\partial \epsilon}{\partial t} = c_{\text{SGS}\epsilon_1} \frac{\epsilon}{k_{\text{SGS}}} [P_{[\kappa_c, \kappa_d]} + F(\kappa_c)] - c_{\text{SGS}\epsilon_2} \frac{\epsilon^2}{k_{\text{SGS}}}, \quad (40)$$

where $c_{\text{SGS}\epsilon_1} = 3/2$ and

$$c_{\text{SGS}\epsilon_2} = \frac{3}{2} - \frac{k_{\text{SGS}}}{(\kappa_d - \kappa_c)E(\kappa_d)} \left[\left(\frac{\mathcal{F}(\kappa_d)}{\epsilon} - 1 \right) - \frac{E(\kappa_d)}{E(\kappa_c)} \left(\frac{\mathcal{F}(\kappa_c)}{\epsilon} - 1 \right) \right]. \quad (41)$$

Setting $\kappa_d \gg \kappa_c$ and $E(\kappa_d) \ll E(\kappa_c)$, Eq. (41) reduces to

$$c_{\text{SGS}\epsilon_2} = \frac{3}{2} - \frac{k_{\text{SGS}}}{\kappa_d E(\kappa_d)} \left(\frac{\mathcal{F}(\kappa_d)}{\epsilon} - 1 \right). \quad (42)$$

In the case of full statistical modeling where $\kappa_c = 0$, Eq. (38) is reduced to the equation

$$\kappa_d = \zeta_d \frac{\epsilon}{k^{3/2}}, \quad (43)$$

where the coefficient ζ_d is a numerical constant chosen such that κ_d is located after the inertial range. By taking the derivative of Eq. (43) with respect to time, using Eqs. (39) and (37), another formulation of the dissipation rate equation is then obtained,

$$\frac{\partial \epsilon}{\partial t} = c_{\epsilon_1} \frac{\epsilon}{k} P_{[0, \infty[} - c_{\epsilon_2} \frac{\epsilon^2}{k}, \quad (44)$$

where $c_{\epsilon_1} = 3/2$ and

$$c_{\epsilon_2} = \frac{3}{2} - \frac{k}{\kappa_d E(\kappa_d)} \left(\frac{\mathcal{F}(\kappa_d)}{\epsilon} - 1 \right). \quad (45)$$

This is in fact the usual ϵ equation used in statistical closures. Equations (42) and (45) show that the coefficients $c_{\text{SGS}\epsilon_2}$ and c_{ϵ_2} are the functions of the spectrum shape. Keeping in mind that the dissipation rate ϵ must remain the same regardless of the location of the wave number κ_c , comparing Eq. (40) with Eq. (44) allows us to express the coefficient $c_{\text{SGS}\epsilon_2}$ in a more convenient form

$$c_{\text{SGS}\epsilon_2} = c_{\epsilon_1} + \frac{k_{\text{SGS}}}{k} (c_{\epsilon_2} - c_{\epsilon_1}). \quad (46)$$

The function k_{SGS}/k which appears in Eq. (46) can be calibrated by referring to the Kolmogorov law of the three-dimensional energy spectrum in the inertial wave number range in nearly equilibrium flows

$$E(\kappa) = C_K \epsilon^{2/3} \kappa^{-5/3}, \quad (47)$$

where $C_K \approx 1.50$ is the Kolmogorov constant. The subgrid-scale turbulent kinetic energy is then estimated by integrating the Kolmogorov law in the wave number range $[\kappa_c, +\infty[$:

$$k_{\text{SGS}} = \int_{\kappa_c}^{\infty} E(\kappa) d\kappa = \frac{3}{2} C_K \epsilon^{2/3} \kappa_c^{-2/3}. \quad (48)$$

Taking into account the expression of the dimensionless wave number $\eta_c = \kappa_c k^{3/2} / \epsilon$ and Eq. (48), the ratio k_{SGS}/k is easily obtained:

$$\frac{k_{\text{SGS}}}{k} = \frac{3C_K}{2} \eta_c^{-2/3}. \quad (49)$$

As a result of interest, Eq. (49) shows that the function k_{SGS}/k is dependent on the parameter $\eta_c^{-2/3}$. The previous result is only valid in the inertial range. It is extended empirically to the general case, taking care to satisfy the limit when k_{SGS} approaches k (i.e., when η_c goes to zero). So, the coefficient $c_{\text{SGS}\epsilon_2}$ in Eq. (46) is modeled taking account of Eq. (49). The empirical choice is proposed as

$$c_{\text{SGS}\epsilon_2} = c_{\epsilon_1} + \frac{c_{\epsilon_2} - c_{\epsilon_1}}{1 + \beta_\eta \eta_c^{2/3}}, \quad (50)$$

where β_η is a numerical constant which takes the theoretical value $\beta_\eta = 2/3 C_K \approx 0.444$ in order to satisfy the correct asymptotic behavior in $\eta_c^{-2/3}$ for high values η_c with the limiting conditions:

$$\lim_{\eta_c \rightarrow 0} c_{\text{SGS}\epsilon_2}(\eta_c) = c_{\epsilon_2},$$

$$\lim_{\eta_c \rightarrow \infty} c_{\text{SGS}\epsilon_2}(\eta_c) = c_{\epsilon_1}.$$

In the limit of full statistical modeling, $k_{\text{SGS}} \rightarrow k$ and the usual RSM model is recovered while in the limit $k_{\text{SGS}} \rightarrow 0$, the subgrid-scale energy is not maintained due to the fact that $c_{\text{SGS}\epsilon_2} \rightarrow c_{\epsilon_1}$ and the model behaves like a DNS (but the model becomes useless!). For nonhomogeneous flows, the convection and diffusion terms are embedded in Eq. (40). Then, also taking into account low Reynolds number terms, the modeled equation of the dissipation rate can be written as follows:

$$\frac{\partial}{\partial t}(\bar{\rho}\epsilon) + \frac{\partial}{\partial x_j}(\bar{\rho}\epsilon\tilde{u}_j) = c_{\epsilon_1} \frac{\epsilon}{k_{\text{SGS}}} \frac{P_{mm}}{2} - c_{\text{SGS}\epsilon_2} \bar{\rho} \frac{\tilde{\epsilon}\epsilon}{k_{\text{SGS}}} + J_\epsilon, \quad (51)$$

where

$$J_\epsilon = \frac{\partial}{\partial x_j} \left(\bar{\mu} \frac{\partial \epsilon}{\partial x_j} + c_\epsilon \bar{\rho} \frac{k_{\text{SGS}}}{\epsilon} (\tau_{jm})_{\text{SGS}} \frac{\partial \epsilon}{\partial x_m} \right) \quad (52)$$

and

$$\tilde{\epsilon} = \epsilon - 2\nu \left(\frac{\partial \sqrt{k_{\text{SGS}}}}{\partial x_n} \right)^2. \quad (53)$$

The values of the numerical coefficients in Eq. (51) are the following: $c_{\epsilon_1} = 1.45$, $c_{\epsilon_2} = 1.9$, and $c_\epsilon = 0.18$. Note that empirical terms incorporated in the original model of Launder and Shima¹⁶ regarding the coefficient c_{ϵ_1} have been suppressed in order not to alter the rationale of the model. Intuitively, it is obvious that the usual ϵ equation used in statistical modeling in which the whole spectrum is modeled cannot be used without modification in LES in which just a part of the spectrum is modeled. This modification is made here through a variation of the coefficient $c_{\text{SGS}\epsilon_2}$. This is the main feature of the present LES model which is basically different from an URANS approach. To achieve the complete closure of the equations, the turbulent heat flux is computed as follows:

$$\overline{h''u''_i} = - \frac{c_\mu k_{\text{SGS}}^2}{\epsilon} \frac{c_p}{P_{r_{\text{SGS}}}} \frac{\partial \bar{T}}{\partial x_i}, \quad (54)$$

where c_p and $P_{r_{\text{SGS}}}$ are the specific heat at constant pressure and the subgrid-scale turbulent Prandtl number, respectively, and c_μ is a constant coefficient setting to 0.09.

B. Practical formulation

In a practical formulation for the case of wall bounded flows, the length scale can be computed using the normal distance to the wall $L = Kx_3$, where K is the Von Kármán constant. In that condition, we use the alternative dimensionless wave number $\mathcal{N}_c = \kappa_c L$ instead of the previous wave number $\eta_c = \kappa_c k^{3/2} / \epsilon$ and we introduce modified coefficients $\alpha_{\mathcal{N}}$ and $\beta_{\mathcal{N}}$ in Eqs. (19) and (50). This simplified approach avoids the calculation of the total turbulence energy involved in the expression of η_c at every time step during the simula-

tion. In that framework, the alternative functions of the subgrid-scale turbulence model are written in the following way:

$$c_{\text{SGS}\epsilon_1} = \frac{1 + \alpha_{\mathcal{N}} \mathcal{N}_c^2}{1 + \mathcal{N}_c^2} c_1 \quad (55)$$

and

$$c_{\text{SGS}\epsilon_2} = c_{\epsilon_1} + \frac{c_{\epsilon_2} - c_{\epsilon_1}}{1 + \beta_{\mathcal{N}} \mathcal{N}_c^{2/3}}. \quad (56)$$

The order of magnitude of the new coefficient $\beta_{\mathcal{N}}$ is then obtained by reference to the logarithmic layer. Considering that $k \approx a_k u_\tau^2$ where $a_k \approx 3.3$ and that $\epsilon \approx u_\tau^3 / Kx_3$ where u_τ is the friction velocity, one can easily obtain the relation $\eta_c = a_k^{3/2} \mathcal{N}_c$ which leads to the theoretical value $\beta_{\mathcal{N}} = 2a_k / 3C_K \approx 1.466$. The cutoff wave number κ_c is approximated by the filter width:

$$\kappa_c = \frac{\pi}{(\Delta_1 \Delta_2 \Delta_3)^{1/3}}. \quad (57)$$

The large-scale part of the Reynolds stress is given by

$$(\tau_{ij})_{\text{LES}} = \langle \bar{u}_i \bar{u}_j \rangle - \langle \bar{u}_i \rangle \langle \bar{u}_j \rangle, \quad (58)$$

so that the total Reynolds stress τ_{is} is calculated as the sum of the subgrid and large-scale parts:

$$\tau_{ij} = (\tau_{ij})_{\text{SGS}} + (\tau_{ij})_{\text{LES}}. \quad (59)$$

C. Realizability conditions for the model

The subgrid-scale stress tensor $(\tau_{ij})_{\text{SGS}}$ computed by the modeled transport equation (14) must satisfy the realizability conditions which imply non-negative values of the three principal invariants I_i that appear in the characteristic polynomial $P(\lambda) = \lambda^3 - I_1 \lambda^2 + I_2 \lambda - I_3$ of the matrix formed by the components $(\tau_{ij})_{\text{SGS}}$.²⁹

$$I_1 = (\tau_{ii})_{\text{SGS}} \geq 0, \quad (60)$$

$$I_2 = \frac{1}{2} [(\tau_{ii})_{\text{SGS}} (\tau_{jj})_{\text{SGS}} - (\tau_{ij})_{\text{SGS}} (\tau_{ji})_{\text{SGS}}] \geq 0, \quad (61)$$

$$I_3 = \frac{1}{6} [(\tau_{ii})_{\text{SGS}} (\tau_{jj})_{\text{SGS}} (\tau_{kk})_{\text{SGS}} - 3(\tau_{kk})_{\text{SGS}} (\tau_{ij})_{\text{SGS}} (\tau_{ji})_{\text{SGS}} + 2(\tau_{ij})_{\text{SGS}} (\tau_{jk})_{\text{SGS}} (\tau_{ki})_{\text{SGS}}] \geq 0. \quad (62)$$

It is easier to examine the question of realizability in a coordinate system aligned with the principal axes of the subgrid-scale stress tensor. For practical reasons, it is also more convenient to analyze the weak form of realizability²⁹ which requires that when a principal subgrid-scale stress component vanishes, its time derivative must be positive. This ensures that negative energy component cannot occur when this constraint is satisfied. Although the basis of the principal axes of the subgrid-scale stress tensor is rotating in time, Speziale *et al.*³⁰ have shown that the first derivative constraint takes the same formulation in the principal axes. So that the modeled transport equation (14) of the turbulent stress component $(\tau_{\alpha\alpha})_{\text{SGS}}$ can be written as

TABLE II. Simulation parameters for the fully developed turbulent channel flow.

Case	N_1	N_2	N_3	L_1/δ	L_2/δ	Δ_1/δ	Δ_2/δ	Δ_{3c}/δ	Δ_1^+	Δ_2^+	Δ_{3c}^+
DNS ^a	256	192	193	π	$\pi/2$	0.012	0.008	0.008	10.0	6.5	6.5
Present LES 1	16	32	64	2	2	0.133	0.065	0.038	105.3	50.9	30.0
Present LES 2	32	64	84	2	2	0.065	0.032	0.029	50.9	25.1	23.0

^aRef. 19.

$$\begin{aligned} & \frac{\partial}{\partial t} [\bar{\rho}(\tau_{\alpha\alpha})_{\text{SGS}}] + \frac{\partial}{\partial x_\beta} [\overline{\bar{\rho}(\tau_{\alpha\alpha})_{\text{SGS}} \tilde{u}_\beta}] \\ &= P_{\alpha\alpha} - \frac{2}{3} \bar{\rho} \epsilon - c_{\text{SGS}1} \bar{\rho} \frac{\epsilon}{k_{\text{SGS}}} \left[(\tau_{\alpha\alpha})_{\text{SGS}} - \frac{2}{3} k_{\text{SGS}} \right] \\ & \quad - c_2 \left(P_{\alpha\alpha} - \frac{1}{3} P_{\beta\beta} \right), \end{aligned} \quad (63)$$

where the Einstein summation convention is suspended for indices $\alpha\alpha$. The diffusion term as well as the reflection term are not considered. When the stress component $(\tau_{\alpha\alpha})_{\text{SGS}}$ vanishes, it can be shown that the production term $P_{\alpha\alpha}$ is zero so that the weak realizability condition implies

$$c_{\text{SGS}1} \geq 1 - c_2 \frac{P_{\beta\beta}}{2\bar{\rho}\epsilon}. \quad (64)$$

Due to the expressions of the coefficients $c_{\text{SGS}1}$ in Eq. (19) and c_2 in Table I, Eq. (64) is verified when the production term $P_{\beta\beta}$ of the turbulent kinetic energy is positive. This corresponds to the usual case of flow physics and ensures, therefore, that the weak realizability constraint is satisfied, as it was previously demonstrated for the statistical RSM model.²

IV. NUMERICAL METHOD

The finite volume technique is adopted in the present code for solving the full transport equations of the mass density, the momentum, the total energy, the subgrid-scale stresses, and the dissipation rate. The fluxes are evaluated at the cell interfaces, whereas the unknown variables are calculated at the center of each cell. The vector of the aerodynamic variables

$$U = [\bar{\rho}, \bar{\rho} \tilde{u}_1, \bar{\rho} \tilde{u}_2, \bar{\rho} \tilde{u}_3, \bar{\rho} \tilde{E}]^t \quad (65)$$

is solved using a centered numerical scheme of second- or fourth-order accuracy in space discretization. The vector T_{SGS} of the turbulent subgrid-scale variables

$$T_{\text{SGS}} = [(\tau_{11})_{\text{SGS}}, (\tau_{12})_{\text{SGS}}, (\tau_{13})_{\text{SGS}}, (\tau_{22})_{\text{SGS}}, (\tau_{23})_{\text{SGS}}, (\tau_{33})_{\text{SGS}}, \rho \epsilon]^t \quad (66)$$

is solved by a noncentered numerical scheme of second-order accuracy in space discretization. The governing equations are integrated explicitly in time using a three-step Runge–Kutta scheme which is well appropriate for simulating unsteady flows. The source terms are linearized to avoid numerical instabilities. The numerical solver has been previously tested on channel flows.³¹ In the present study, the top hat filter has been considered.

V. LES OF FULLY DEVELOPED TURBULENT CHANNEL FLOW

This flow is chosen as a preliminary test case for the proposed approach. The sizes of the channel in the streamwise, spanwise, and normal directions along the axes x_1 , x_2 , x_3 , respectively, are given in Table II. In this table, N_i is the number of grid points, L_i is the length of the computational box, Δ_i ($i=1, 2$) is the uniform spacing, and Δ_{ic} ($i=3$) is the maximum spacing in the center of the channel.

Numerical simulations are performed on coarse and refined meshes requiring $16 \times 32 \times 64 = 32\,768$ grids and $32 \times 64 \times 84 = 172\,032$ grids with different spacings Δ_i . This choice is motivated by the necessity of checking the grid independence of the solution on the numerical point of view as well as the consistency of the subgrid scale model when the filter width is changed. In the normal direction to the wall, the grid points are distributed in nonuniform spacing with refinement near the wall according to the transformation

$$x_{3j} = \frac{1}{2} \tanh[\xi_j \operatorname{artanh} a], \quad (67)$$

where

$$\xi_j = -1 + 2(j-1)/(N_3-1) \quad (j=1, 2, \dots, N_3). \quad (68)$$

Here $a=0.98\,346$ and $N_3=64$ or 84 . The mesh is uniform in the two remaining directions. More precisely, the first point of the mesh in the direction normal to the wall is located at the dimensionless distance $\Delta_3^+ = \Delta_3 u_\tau / \nu = 0.5$, whereas the uniform dimensionless spacings in the other directions are for case 1, $\Delta_1^+ = 105.3$, $\Delta_2^+ = 50.9$ and for case 2, $\Delta_1^+ = 50.9$, $\Delta_2^+ = 25.1$ as indicated in Table II. The numerical simulation of fully developed turbulent channel flow is compared with the data obtained by direct numerical simulation¹⁹ for a Reynolds number $R_\tau = \rho_\tau \mu_\tau \delta / 2\mu = 395$, based on the averaged friction density ρ_τ , the averaged friction velocity u_τ and the channel half-width $\delta/2$. Periodic boundary conditions are applied in the streamwise and spanwise directions whereas a no-slip velocity condition is imposed at the walls. The periodic boundary condition in the streamwise direction required the introduction of a constant pressure gradient term $G = 2\rho_\tau \mu_\tau^2 / \delta$ in both the momentum and energy equations for balancing the friction at the walls. The flow conditions selected for the simulations are nominally atmospheric air. The wall temperature T_w is taken as 300 K. Zero turbulent subgrid kinetic energy and the dissipation rate value $\epsilon_w = 2\nu(\partial\sqrt{k_{\text{SGS}}}/\partial x_3)^2$ are specified at the walls. The initial flowfield is composed of an isotropic turbulence field³² superposed to an anisotropic set of eddies. The effect of the eddies is to increase the turbulent production term resulting from the shear stress. The anisotropic set of eddies is chosen such

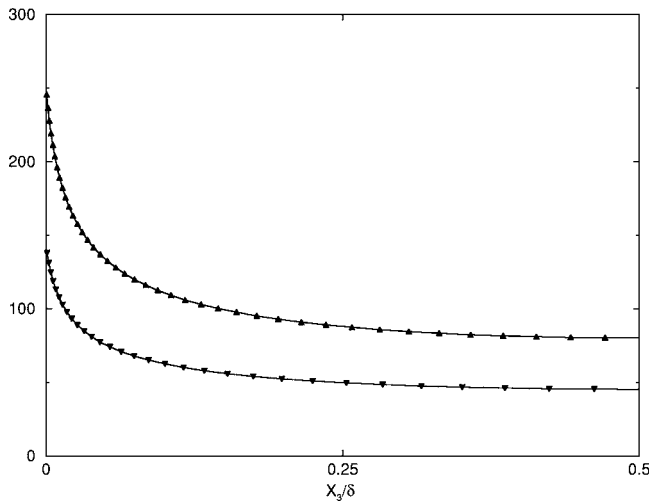


FIG. 1. Dimensionless cutoff wave number $\kappa_c \delta = \pi \delta / \Delta$; \blacktriangledown , LES1; \blacktriangle , LES2. $R_\tau = 395$.

that the ensuing mean shear stress reach a level comparable to the one prevailing in usual channel flow. As a consequence the development of the turbulent field is enhanced and the statistical convergence of the LES simulation is speeded up. Although this practice is not necessary to develop a numerical simulation, it does help the convergence.

Several trial and error tests have been made for selecting appropriate values for the two model coefficients α_N and β_N . These tests have led to the optimized coefficient values $\alpha_N = 1.5$ and $\beta_N = 0.5$. Figure 1 describes the evolution of the cutoff wave number $\kappa_c = \pi / \Delta$, where $\Delta = (\Delta_1 \Delta_2 \Delta_3)^{1/3}$ versus the normal distance to the wall x_3 which depend on the mesh distribution for the two grids. Figure 2 shows the evolution of the dimensionless cutoff wave number \mathcal{N}_c versus the distance normal to the wall. This function is increasing with the distance from the wall to the center of the channel. Figure 3 describes the variations of the function c_{SGS1} / c_1 versus the normal distance x_3 . As a consequence of Eq. (19), this function is increasing with the wall distance in order to strengthen the return to isotropy at greater wave numbers.

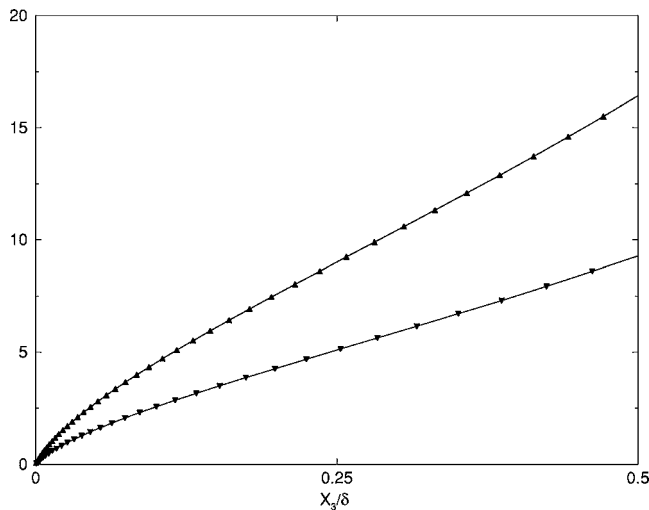


FIG. 2. Dimensionless parameter $\mathcal{N}_c = \kappa_c L$; \blacktriangledown , LES1; \blacktriangle , LES2. $R_\tau = 395$.

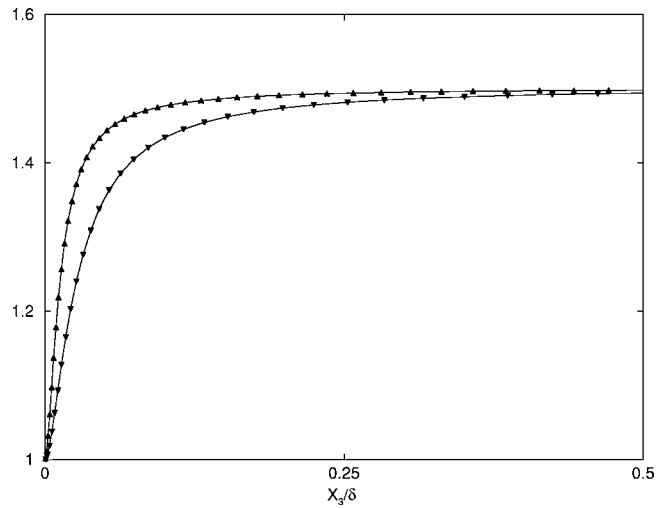


FIG. 3. Normalized function c_{SGS1} / c_1 ; \blacktriangledown , LES1; \blacktriangle , LES2. $R_\tau = 395$.

Figure 4 shows the evolution of the coefficient $c_{SGS\epsilon_2}$ versus the wall distance x_3 . For the coarse and refined meshes, $c_{SGS\epsilon_2}$ varies in the ranges $[1.60, 1.9]$ and $[1.55, 1.9]$, respectively. These values stay nicely in scale between the two limiting values $c_{\epsilon_1} = 1.45$ and $c_{\epsilon_2} = 1.9$ according to Eq. (50). The function $c_{SGS\epsilon_2}$ goes to the limit c_{ϵ_2} near the walls because the parameter \mathcal{N}_c tends to zero in that region, and is decreased when moving to the centerline of the channel. This result means that the subgrid-scale model varies continuously from quasi-URANS to a LES model and behaves more or less like the RSM model very close to the wall, although the mesh is very refined ($\Delta_3^+ = 0.5$).

Figure 5 shows the profiles of the mean velocity (statistical average) $\langle u_1 \rangle / u_\tau$ in logarithmic coordinate $x_3^+ = x_3 u_\tau / \nu$ for the coarse and refined meshes. One can observe that the velocities agree very well with the DNS data. Figure 6 describes the distributions of the streamwise, spanwise, and normal normalized subgrid stresses, $\langle (\tau_{ii})_{SGS} \rangle^{1/2} / u_\tau$ for the coarse and refined meshes. In the same way, Fig. 7 presents the evolutions of the streamwise, spanwise, and normal

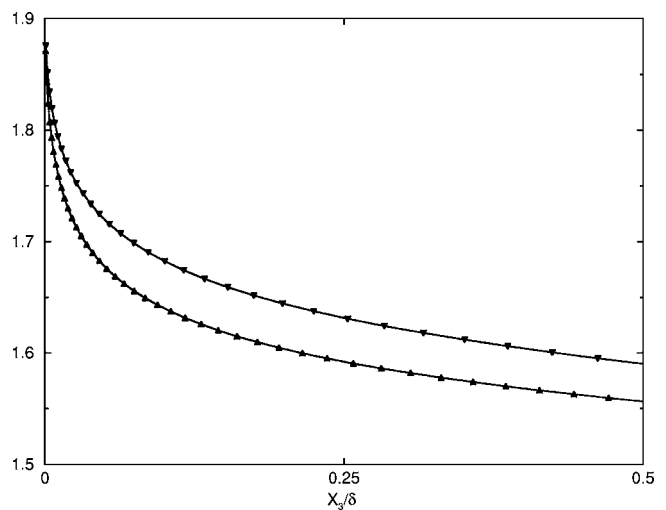


FIG. 4. Subgrid-scale coefficient $c_{SGS\epsilon_2}$; \blacktriangledown , LES1; \blacktriangle , LES2.

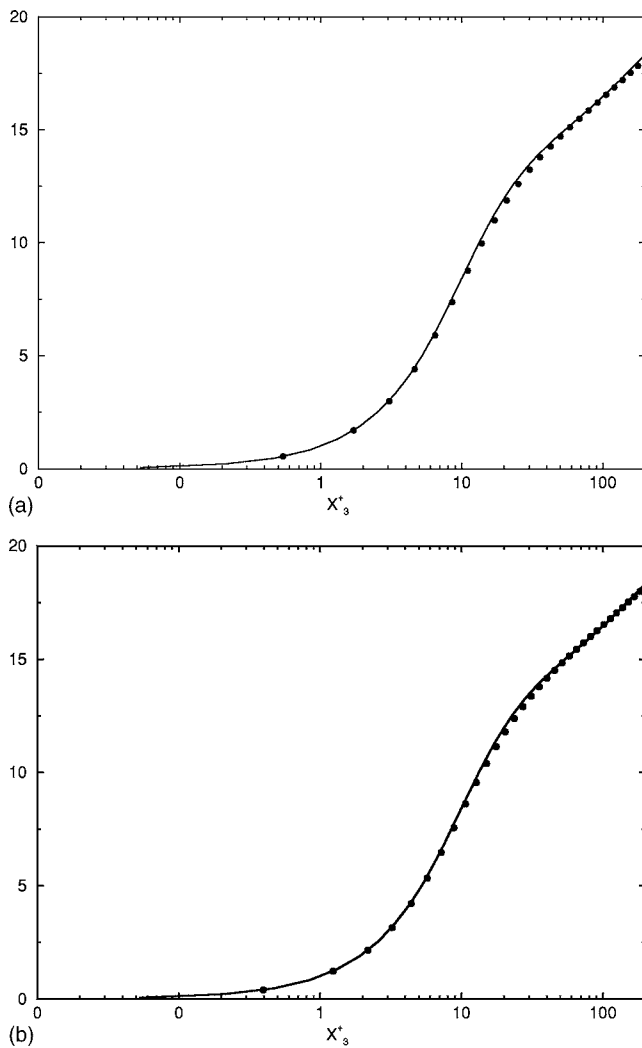


FIG. 5. Mean velocity profile. $\langle u_1 \rangle / u_\tau$ in logarithmic coordinate; \bullet , (a) LES 1, (b) LES 2; —, DNS. $R_\tau=395$.

large-scale stresses $\langle (\tau_{ii})_{\text{LES}} \rangle^{1/2} / u_\tau$. The curves present regular shapes characterized by the peaks of turbulence intensity close to the walls. A good degree of symmetry for the large-scale stresses is reached at the statistical convergence. As results of interest, Fig. 6 indicates that the subgrid-scale stresses are indeed anisotropic in the vicinity of the walls. This remark demonstrates the usefulness of the present LES model based on the transport equations for the subgrid-scale stresses. As expected, the proportion of the turbulence distributed in the subgrid part and large-scale part is governed by the mesh size. For the coarse mesh, the subgrid part presents higher intensity than those observed for the refined mesh, whereas the large-scale part shows lower intensity than those reached for the refined mesh. The sharing out of turbulence energy among the subgrid and resolved turbulence scales (see Fig. 7) for the coarse and refined mesh evolves according to the analytical behavior of the model which is governed by Eq. (50). In the center of the channel, the part of energy in the resolved scales is larger than the part of energy in the subgrid scales. Figure 8 shows the evolutions of the normalized total Reynolds stresses computed as the sum of the subgrid- and large-scale parts $[\langle (\tau_{ii})_{\text{SGS}} \rangle$

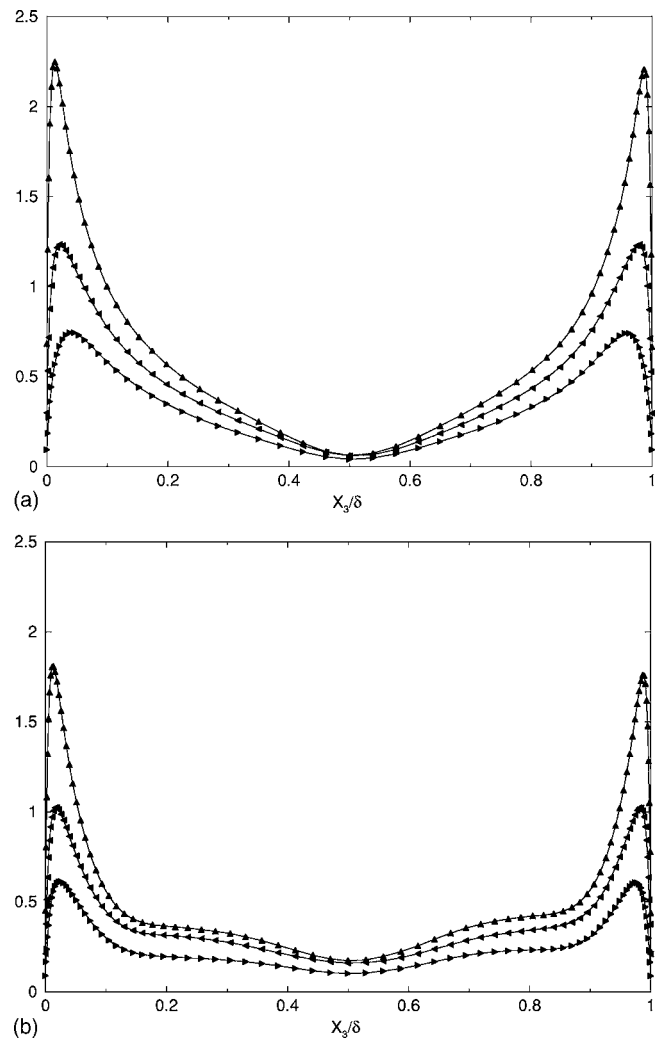


FIG. 6. Turbulent subgrid-scale stresses $\langle (\tau_{ii})_{\text{SGS}} \rangle^{1/2} / u_\tau$. (a) LES 1; (b) LES 2; \blacktriangle , $i=1$; \bullet , $i=2$; \blacktriangleright , $i=3$. $R_\tau=395$.

$+\langle (\tau_{ii})_{\text{LES}} \rangle]^{1/2} / u_\tau$ ($i=1,2,3$) for the two different meshes with comparisons with the DNS data. For the LES simulation performed on the coarse mesh, a fair agreement with the DNS data is observed but the turbulent stresses appear slightly overpredicted in the channel although the intensity of the turbulent peak close to the walls is well reproduced. This remaining discrepancy with the DNS data results probably from the numerical scheme diffusion effects which are generated by the mesh discretization errors for such a very coarse grid. For the refined mesh which provides better numerical resolution, a very good agreement is obtained with the DNS data. These figures also show the good behavior of the model when the filter width is changed. Figure 9 is related to the distributions of the normalized shear stress, respectively, for the subgrid- and large-scale parts, $\langle (\tau_{13})_{\text{SGS}} \rangle / u_\tau$ and $\langle (\tau_{13})_{\text{LES}} \rangle / u_\tau$ for the coarse and refined meshes. Both the subgrid- and large-scale turbulent shear stresses, are perfectly antisymmetric through the channel cross section without any spurious oscillation. For the refined mesh, the SGS part is smaller than the LES part while the reverse situation occurs for the coarse mesh. As for the normal stresses, the SGS part of the shear stress is larger for the

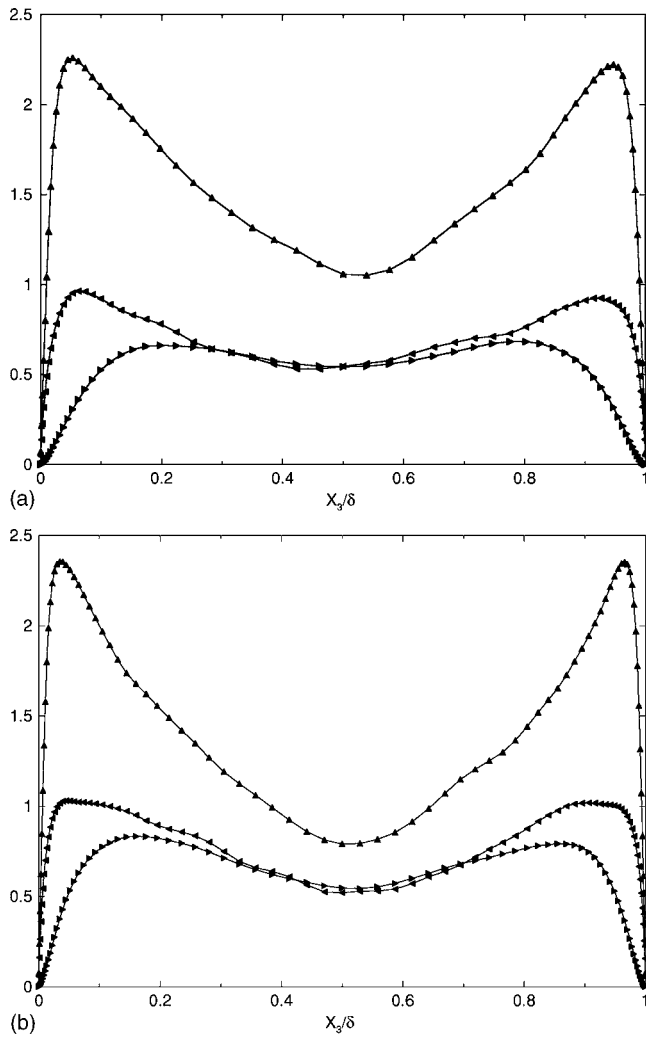


FIG. 7. Turbulent large scale stresses $\langle(\tau_{ii})_{LES}^{1/2}\rangle/u_\tau$. (a) LES 1; (b) LES 2; \blacktriangle , $i=1$; \blacksquare , $i=2$; \blacktriangleright , $i=3$. $R_\tau=395$.

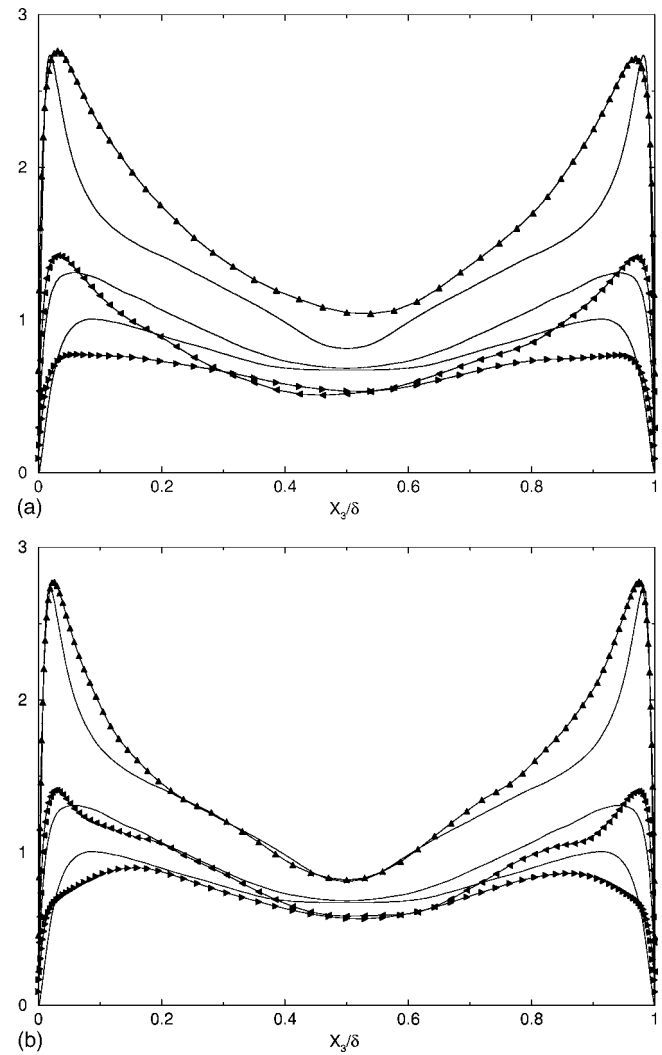


FIG. 8. Turbulent Reynolds stresses $[\langle(\tau_{ii})_{SGS}\rangle + \langle(\tau_{ii})_{LES}\rangle]^{1/2}/u_\tau$. (a) LES 1; (b) LES 2; \blacktriangle , $i=1$; \blacksquare , $i=2$; \blacktriangleright , $i=3$; —, DNS. $R_\tau=395$.

coarse mesh than the one observed for the refined mesh. Figure 10 shows the evolution of the total shear stress $[\langle(\tau_{13})_{SGS}\rangle + \langle(\tau_{13})_{LES}\rangle]/u_\tau$ for the coarse and refined meshes. For both simulations, excellent agreements with the DNS data are observed, although the distributions between the SGS and LES scale parts are quite different between the two simulations. These two figures also demonstrate that the statistical convergence is correctly achieved.

Equation (64) has demonstrated that the subgrid-scale model satisfies the weak form of realizability conditions. As an illustration of that result, the plane formed by the second and third subgrid-scale invariants A_2-A_3 of Lumley is used to check the realizability constraint in a particular case. Lumley³³ has shown that the possible turbulence states are located inside a region bounded by a curvilinear triangle formed by the straight line of the two-dimensional state verifying the equation $A_3-A_2+8/9=0$ and by the two curves of the axisymmetric states verifying the equation $|A_2|=6^{1/3}A_3^{2/3}$. Figure 11 shows the calculated trajectories using the turbulent subgrid-scale model in the plane of the subgrid-scale invariants. The solution trajectories are computed along a straight line normal to the wall in a cross section of the

channel. As expected, the solution trajectories remain inside the curvilinear triangle of realizability, so that the realizability conditions (60)–(62) are well satisfied. When moving from the two rigid walls toward the centerline of the channel, the trajectories depart from the upper region of the triangle and run along similar curves then arriving close to the origin where a quasi-isotropic state is reached.

Figure 12 shows the evolutions of two-point correlation functions

$$R_{ii}(x_1, x_2, x_3) = \frac{\langle u_i''(x_1, x_2, x_3) u_i''(x_1 + r_1, x_2, x_3) \rangle_{LES}}{\langle u_i''^2(x_1, x_2, x_3) \rangle_{LES}} \quad (69)$$

for $i=1, 2, 3$ (no summation), R_{11} , R_{22} , and R_{33} , versus the streamwise distance x_1 where r_1 ranges from 0 to δ . The correlations are plotted in the center height of the channel $x_3=\delta$. The regular decay of the curves confirms that the box size can be considered as adequate because the tensor correlations do return to zero for $r_1=\delta$. Considering that these calculations are time consuming, we indeed choose the minimal size of the box ensuring vanishing of correlations. Moreover, a previous trial numerical simulation using a box twice

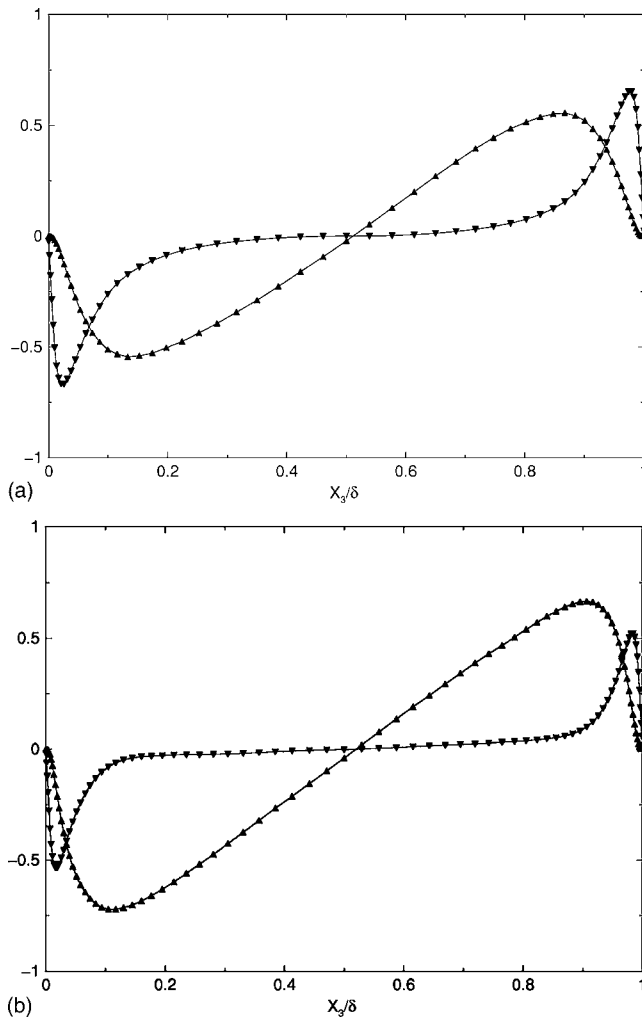


FIG. 9. Turbulent subgrid-scale shear stress $\langle(\tau_{13})_{SGS}\rangle/u_\tau$ and turbulent large grid-scale shear stress $\langle(\tau_{13})_{LES}\rangle/u_\tau$. (a) LES 1; (b) LES 2; ∇ , SGS; \blacktriangle , LES. $R_\tau=395$.

as large as in the streamwise direction for an almost similar grid definition has led to nearly identical solutions. As already observed with LES simulations of Moin and Kim⁶ (cf. Fig. 6), the correlation for the velocity in the streamwise direction R_{11} is larger than the corresponding transverse correlations R_{22} or R_{33} . The slow decay of R_{11} for increasing r_1 indicates the presence of highly elongated eddies in the streamwise direction. Figure 13 shows the isosurfaces of the instantaneous vorticity vector $\omega_i \nu / u_\tau^2$, where $\omega_i = \epsilon_{ijk} \partial u_k / \partial x_j$ for $i=1,2,3$ in the streamwise, spanwise, and normal directions. According to the experimental flow observations,³⁴ it can be seen that the streamwise vortices which are a central dynamical element in wall turbulence are reproduced by the LES simulation with qualitative agreement. The isosurface structures associated to the streamwise and normal components of the vorticity vector appear less organized than those associated to the spanwise component which are more elongated in the streamwise direction. The spanwise component of vorticity fluctuations ω_2 of higher intensity than the other components attains its maximum at the wall and then decreases toward the center of the channel. Two values for $|\omega_2| \nu / u_\tau^2 = 0.1$ are considered in Fig. 13(b). It is obvious that

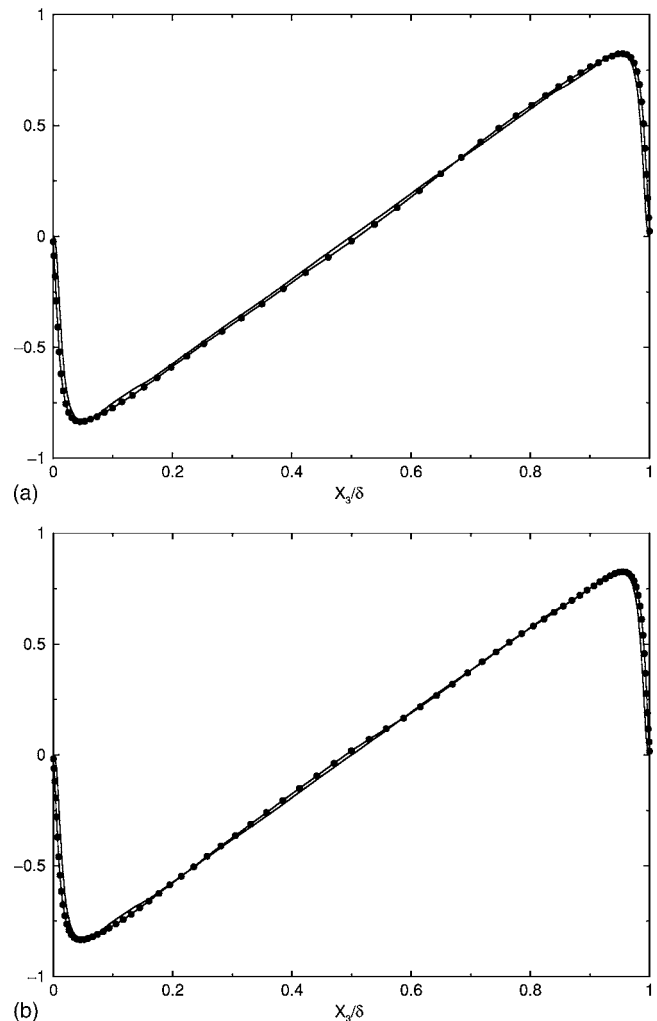


FIG. 10. Turbulent shear stress $[\langle(\tau_{13})_{SGS}\rangle + \langle(\tau_{13})_{LES}\rangle]/u_\tau^2$. \bullet , (a) LES 1; (b) LES 2; —, DNS. $R_\tau=395$.

more quantitative structural information requires a DNS mesh resolution to be properly computed. However, it can be roughly estimated through two-dimensional (2D) view from Fig. 13(b) that the center of the streamwise vortex is located on the average at $x_3^+ \approx 20$ in agreement with the DNS data.³⁵ But more insight shows that the spanwise distance between two counterrotating vortex pairs is of the order $80u_\tau/\nu$ ($x_3^+ = 80$) which is somewhat overpredicted in comparison with experimental or DNS data ($50u_\tau/\nu$). The present LES mesh resolution is probably not really sufficient in the spanwise direction to get a fine definition of longitudinal structures. However, it is remarkable that the present calculation, in spite of its coarse grid, succeeded to obtain a good qualitative prediction of these structures. The isosurface of large-scale pressure fluctuations defined as $\hat{P} = \bar{P} - \langle P \rangle$, for the dimensionless value $\hat{P}/\rho_w u_\tau^2 = -2.5$ are plotted in Fig. 14. Local low pressure regions which correspond to the cores of strong vortical fluid motion are visible. The larger flow structures seem sometimes to be composed of an ensemble of hairpin vortices that are inclined at the wall.

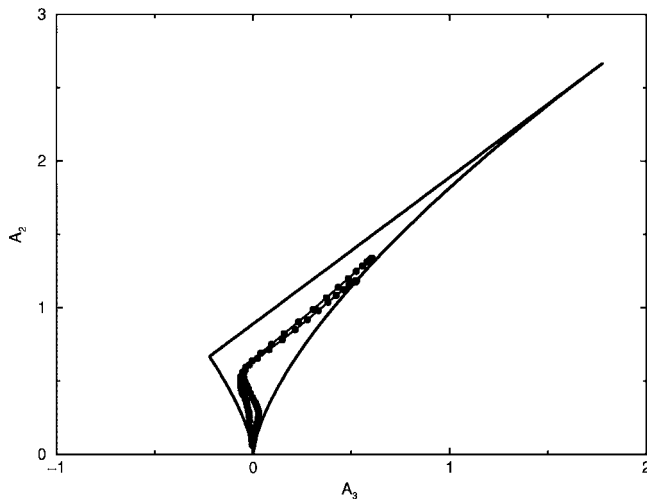


FIG. 11. Solution trajectories produced by the turbulent subgrid-scale model in fully developed channel flow projected onto the second-invariant/third-subgrid-scale invariant plane. ●, LES 1. $R_\tau=395$.

VI. LES OF CHANNEL FLOW WITH WALL INJECTION

The objective is to investigate the flow in a channel with appreciable fluid injection through a permeable wall as sketched in Fig. 15. The presence of wall injection is encountered in the combustion induced flowfields in solid propellant rocket motors where the mass injection simulates the propellant burning.^{36,37} Modeling such flow for predicting the ballistics of the rocket is a challenging task because the flow evolves from a laminar to a turbulent regime in the motor chamber due to the transition of the mean axial direction. Moreover, in comparison with the shear stress of wall-bounded flow, the mass transfer modifies the shear stress distribution across the flow which is continuously evolving. The literature indicates that a first-order statistical model such as $k-\epsilon$ model fails to predict such complex flows³⁸ contrary to a second-order model which is more appropriate.³⁹ This fact has been confirmed recently in Refs. 2 and 20 using a $k-\epsilon$ and an advanced Reynolds stress

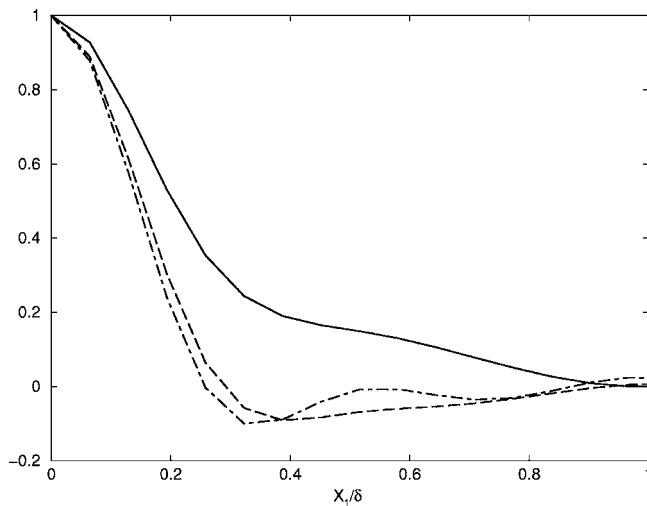
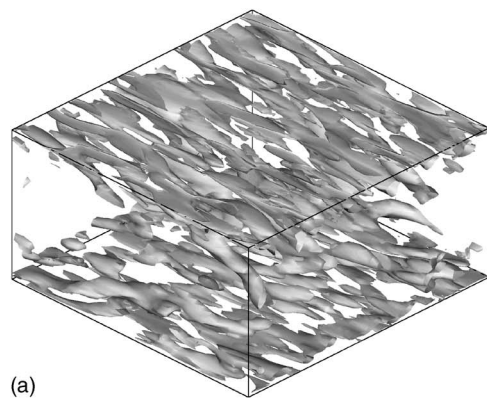
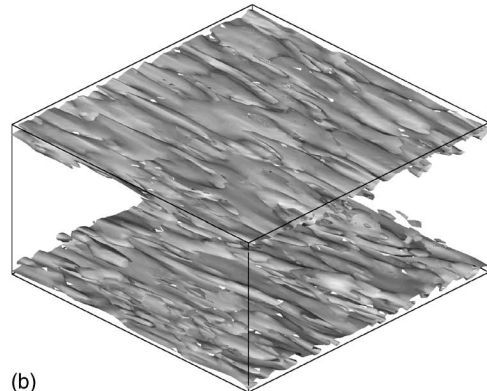


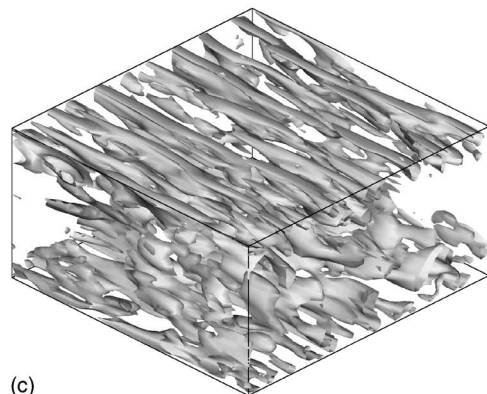
FIG. 12. Streamwise two-point correlation function. — R_{11} ; -- R_{22} ; - . - R_{33} . $x_3^+ = 390$, $x_3 = \delta$; LES 2. $R_\tau = 395$.



(a)



(b)



(c)

FIG. 13. Isosurfaces of instantaneous vorticity vector $\omega_i = \epsilon_{ijk} \partial u_k / \partial x_j$. (a) Streamwise direction $\omega_1 v / u_\tau^2 = 0.04$. (b) Spanwise direction $|\omega_2| v / u_\tau^2 = 0.10$. (c) Normal direction $\omega_3 v / u_\tau^2 = 0.03$. case 1. $R_\tau = 395$.

model for injection induced flows. However, the RSM model cannot provide structural information on the flows. LES simulation is another promising route for studying motor internal flows. In the past, Piomelli *et al.*⁴⁰ used a Smagorinsky model to simulate fully turbulent channel flows in a chamber motor. The fluid was injected through the lower wall and removed at the same rate through the upper one, whereas periodic boundary conditions were applied in the inlet and outlet domains. It has been found that injection enhances turbulent fluctuations and decreases the shear stress. More recently, Apte and Yang⁴¹ performed large eddy simulations using a dynamic Smagorinsky model for the flow in a porous chamber with surface mass injection representative of solid rocket motors. In that simulation, a refined mesh ($640 \times 100 \times 140 = 8\,960\,000$ grid points) in the streamwise, span-

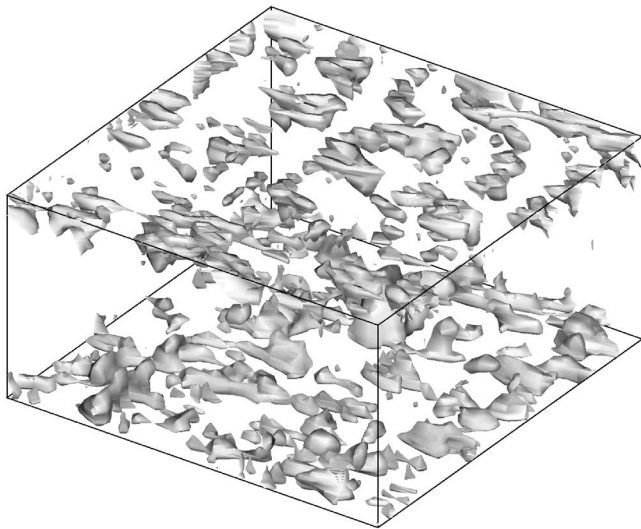


FIG. 14. Isosurfaces of pressure fluctuations. $\hat{P} = \bar{P} - \langle P \rangle$. $\hat{P}/(\rho_w u_\tau^2) = -2.5$; case 1. $R_\tau = 395$.

wise, and normal directions was used. As a result of the simulation, the different flow regimes were successfully reproduced and the turbulence intensity was well predicted. In addition, these authors indicated that the fluid injection enhances the formation of roller-like vortical structure close to the injection surface. The flow appears to be essentially two dimensional up to the midsection of the chamber and becomes three dimensional when the turbulence transition occurs. Note that such a computational simulation cannot be performed easily for practical applications because of the prohibitive CPU time. For that reason, Wasistho and Moser²¹ involved in the center for simulation of advanced rockets program have suggested to apply a model which can match detached eddy simulation near the wall and conventional LES away from the wall. The DES approach is a model of low resolution which derives from the Spalart–Almaras model.¹⁸ This model takes into account a computed length scale which is a function of the mesh size in the wall direction. However, because of its formulation, it is empirically sensitive to the grid spacing refinement. In a first step of their strategy, these authors have performed numerical simulations of fully turbulent channel flows using, respectively, the DES and LES models. Several test cases have been conducted to study the mesh influence. As follows: DES for a coarse mesh $64 \times 32 \times 64$ at $R_\tau = 2000$ (case *D*); LES dynamic model for a refined mesh $64 \times 64 \times 128$ at $R_\tau = 180$ (case *A*) and LES for a coarse mesh at $R_\tau = 1000$ (case *F*). Their results have shown that the DES (case *D*) failed to predict the logarithmic wall layer of the velocity. On the other hand, it was found that the LES performed on the refined mesh (case *A*) produced good results for both the velocity and the turbulent stresses,

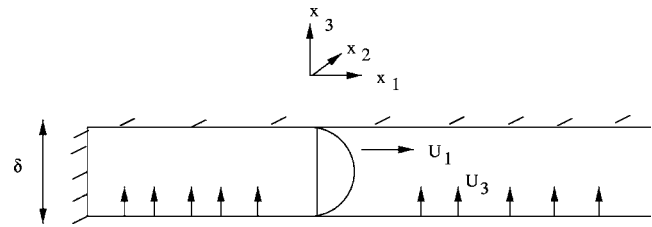


FIG. 15. Schematic of channel flow with fluid injection of Vecla setup.

whereas the LES performed on the coarse mesh (case *F*) overpredicted by a factor 2 the rms stress values. Indeed, these investigations confirm the limitation of DES and LES models in their capacities to reproduce accurately turbulent flows for coarse meshes, so that these authors consider²¹ that new efforts need to be made in that direction for engineering applications. In the present case, one can mention that the new partially integrated transport model has been developed in this aim. This model which allows to bridge URANS and LES methods appears in that line of thought.

The present study is concerned with LES simulation of the flow which develops in the specific experimental setup VECLA made at ONERA.⁴² The setup is composed of a channel bounded by a lower porous plate and an upper impermeable wall. Cold air at 303 K is injected at a high uniform mass flow rate $m = 2.619 \text{ kg/m}^2 \text{ s}$ through a porous material with porosities $8 \mu\text{m}$ or $18 \mu\text{m}$ giving an injection velocity of 1.5 m s^{-1} . Values of the length, the height, and the width of the channel are, respectively, $L_1 = 58.1 \text{ cm}$, $L_2 = 6 \text{ cm}$, and $\delta = 1.03 \text{ cm}$. The pressure at the head end of the channel is 1.5 bars whereas the pressure in the exit section is 1.374 bars. Because of the mass conservation, the flow Reynolds number $R_m = \rho_m u_m \delta / \mu$, based on the bulk density ρ_m , the bulk velocity u_m and the total height δ , varies linearly versus the axial distance of the channel. It ranges from 0 to $\approx 9 \times 10^4$. The injection Reynolds number $R_s = \rho_s u_s \delta / \mu$, defined by the injection density ρ_s , the velocity u_s , the dynamical viscosity μ , at the porous surface, is close to 1600. Experiments in three-dimensional geometry have been carried out by Avalon.⁴² The mean velocity profiles and the Reynolds stress turbulent intensities have been measured in eight sections of the channel located at $x_1 = 3.1, 12, 22, 35, 40, 45, 50,$ and 57 cm with a hot-wire probe. The wire has a length of 2 mm and a diameter of $150 \mu\text{m}$. The bulk velocities u_m passing through these sections are 4.61, 20, 32, 52, 60, 68, 76, and 90 m/s. Periodic boundary conditions are imposed in the spanwise direction for a width domain defined as two-channel heights. A constant pressure boundary condition is applied for the exit section of the channel. Boundary conditions for impermeable walls assume zero velocity and constant temperature, zero turbulent kinetic energy, and the wall dissipation rate value $\epsilon_w = 2\nu(\partial\sqrt{k_{SGS}}/\partial x_2)^2$. For the perme-

TABLE III. Simulation parameters for the channel flow with wall injection.

Case	N_1	N_2	N_3	L_1/δ	L_2/δ	Δ_1/δ	Δ_2/δ	Δ_{3c}/δ
Present LES	400	44	80	56.4	2	0.141	0.045	0.011

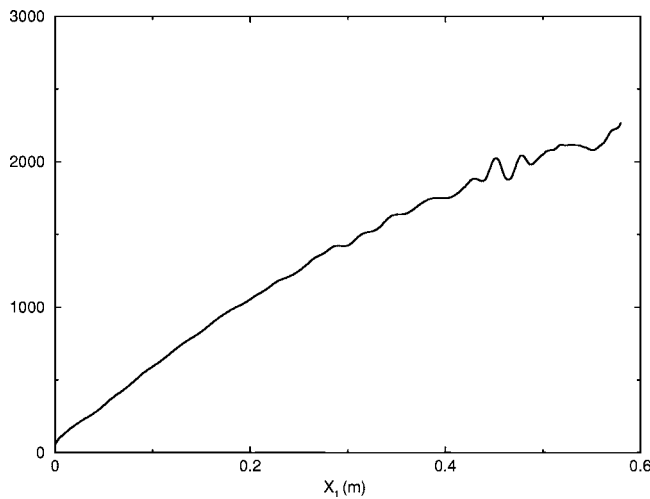


FIG. 16. Axial variation of Reynolds number based on the friction velocity $R_\tau = u_\tau \delta / 2\nu$.

able wall, a constant mass flow rate is imposed at the wall temperature. Taking into account experimental measurements in the immediate vicinity of the permeable wall which show that the velocity follows a Gaussian distribution and that the amplitude of the fluctuating velocity increases with increasing injection velocity,⁴² the boundary conditions are modeled by a twofold hypothesis. It consists in introducing a modeled turbulence intensity level at the wall related to the mean injection velocity defined as $\sigma_s = (\overline{u_2'' u_2''} / \overline{u_s^2})^{1/2}$ in the subgrid turbulence level and to apply a random forcing in time but constant in space, at the surface injection to trigger the turbulence transition in the resolved scale level.

The numerical simulation is performed on a medium mesh composed of $400 \times 44 \times 80 = 1\,408\,000$ grid points in the streamwise, spanwise, and normal directions to the wall. This mesh can be compared with the refined mesh of Apte and Yang⁴¹ for a quasisimilar computational domain. In the present case, a strong decrease in the number of grid points is obtained because of the new subgrid-scale turbulence model. The different ratios Δ_i / δ ($i=1,2$) of the mesh are indicated in Table III. The grid is refined when approaching the permeable and impermeable walls. In order to provide a full resolution for the flow in the wall regions, the smallest grid size at the wall is $25\ \mu\text{m}$, leading to a dimensionless distance for the first grid point from the wall $x_2^+ < 5$. A relatively low turbulence level $\sigma=0.01$ has been considered. The magnitude of the white noise perturbation is 1% to destabilize the large-scale flow.

The statistical mean flow properties are computed over a time period of 10 ms after the unsteady flow convergence. Figure 16 shows the evolution of the Reynolds number $R_\tau = \rho_\tau \mu_\tau \delta / 2\mu$ based on the averaged density ρ_τ and the friction velocity u_τ versus the longitudinal distance of the channel. The averaged friction velocity is defined as $u_\tau = [\frac{1}{2}(u_{\tau w}^2 + u_{\tau s}^2)]^{1/2}$, where $u_{\tau w}$ and $u_{\tau s}$ are the friction velocities computed on the impermeable wall and on the injection surface, respectively. An important flow characteristic is that the Reynolds number ranges from 0 to ≈ 2200 at the exit section of

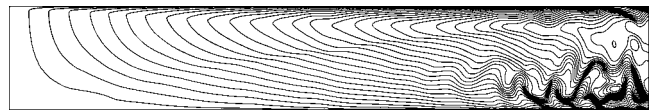


FIG. 17. Snapshots of instantaneous filtered Mach number in the (x_1, x_3) plane, $x_2 / \delta = 1$; $0 < \text{Mach} < 0.34$; $\Delta = 30$.

the channel (395 in the preceding section for the fully developed channel flow).

A. Instantaneous flowfield structures

Figure 17 shows the development of the instantaneous filtered Mach number contours in the plane (x_1, x_3) of the channel. The Mach number ranges from 0 in the head end of the channel to ≈ 0.35 in the exit section. Figures 18 and 19 describe the instantaneous spanwise filtered vorticity $\tilde{\omega}_2 = \partial \tilde{u}_3 / \partial x_1 - \partial \tilde{u}_1 / \partial x_3$, in different planes (x_1, x_3) , (x_1, x_2) of the channel and provide the detail of the flow structures subjected to mass injection, as well as the location of the transition which occurs for $x_1 / \delta \approx 35$. Indeed, in the first part of the channel, the contour lines present a regular behavior in accordance with a quasilaminar flow regime. Then, the contour lines evolve more rapidly due to the natural instabilities which develop from the injection surface. In that region after the transition location, the flow becomes turbulent showing large energy carrying structures arising from the injection surface which are convected by the mean flowfield to the exit. The flow is then characterized by the presence of roll-up vortex structures of large magnitude of vorticity. Because of the injection, it is found that these structures are inclined in the normal direction to the axial flow as previously observed by Apte and Yang.⁴¹ One can notice that these vortices are somewhat different from the elongated streamwise vortices which lie in the impermeable wall region. Figure 19 indicates that the intensity of the vortices in the planes $(x_3 / \delta \approx 0; x_3 / \delta \approx 0.5; x_3 / \delta \approx 1)$ decreases from the injection surface to the center of the channel along a normal distance to the wall. As a result of interest, one can observe that the vortical structures appear two dimensional in the upstream transition location and break down to form three-dimensional structures for $x_1 / \delta > 35$ after the flow transition. Note that the spanwise direction plays an essential role in the vortex-stretching mechanisms and therefore in the prediction of the turbulence intensity. Indeed, previous simulations performed on different meshes taking into account less than 40 planes in the spanwise direction have underpredicted the turbulence intensity of the flow. On the other hand in comparison with the present mesh, the flow intensity remains unchanged when continuing on increasing the spanwise mesh resolution. This result is usually observed for LES simulations. It means that



FIG. 18. Snapshots of spanwise instantaneous filtered vorticity in the (x_1, x_3) plane, $x_2 / \delta = 1$; $-4 \times 10^4\ \text{s}^{-1} < \tilde{\omega} < 4 \times 10^4\ \text{s}^{-1}$; $\Delta = 40$.

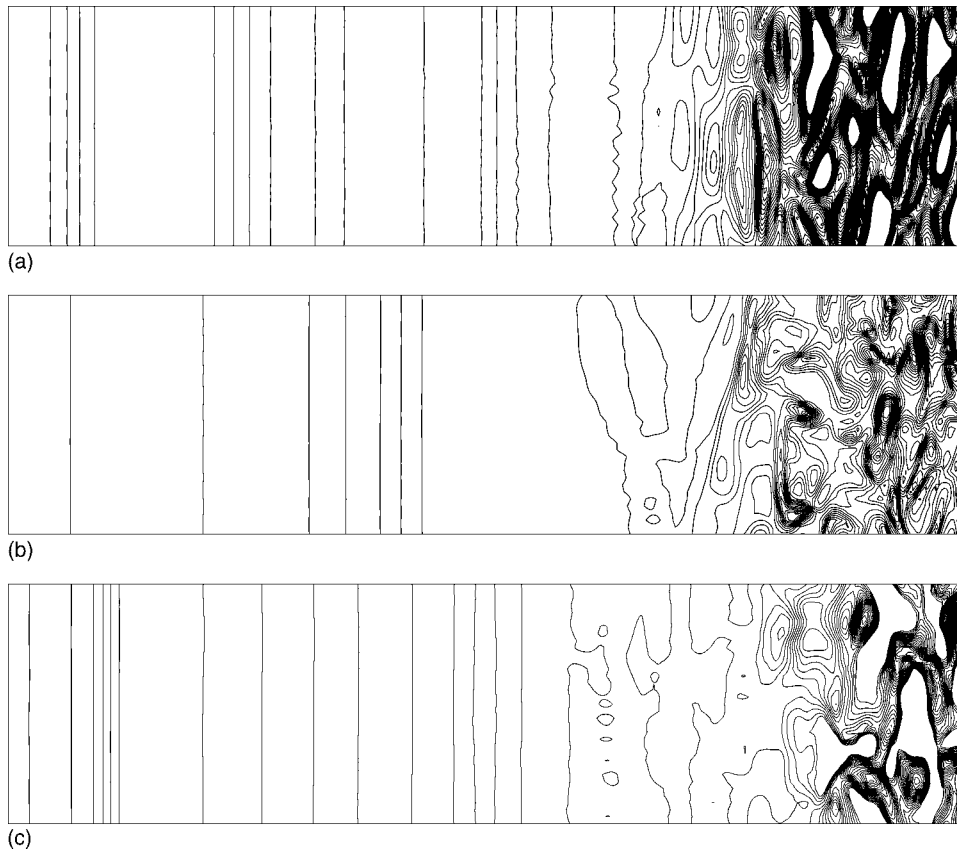


FIG. 19. Snapshots of spanwise instantaneous filtered vorticity in the (x_1, x_2) plane, (a) $x_3/\delta \approx 0$; (b) $x_3/\delta \approx 0.5$; (c) $x_3/\delta \approx 1$; $-4 \times 10^4 \text{ s}^{-1} < \hat{\omega} < 4 \times 10^4 \text{ s}^{-1}$, $\Delta = 40$.

the three-dimensional component plays an essential role in the acting mechanisms of the flow and in particular in the capture of elongated near wall eddies.

B. Mean velocity profiles and turbulence statistics

Figure 20 shows the velocity profiles at different cross sections in the channel. A very good agreement between the LES profiles and the experimental data is obtained. Relative to the permeable wall region, the velocities in the boundary

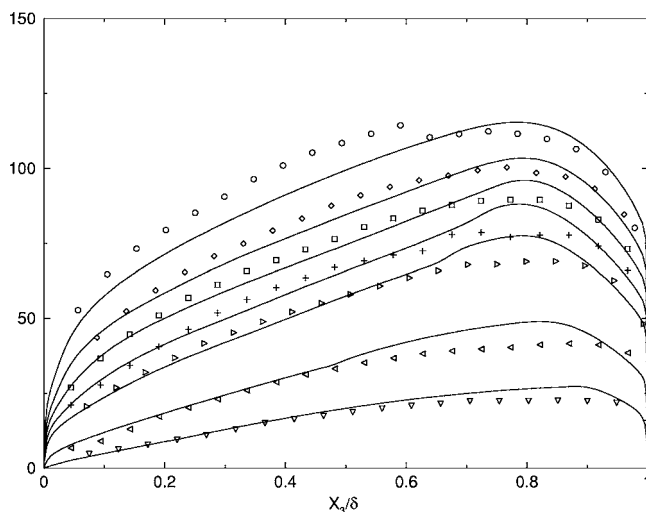


FIG. 20. Mean velocity profiles in different cross sections. Symbols, experimental data; —, LES; 12 cm, ∇ ; 22 cm, \triangleleft ; 35 cm, \triangleright ; 40 cm, $+$; 45 cm, \square ; 50 cm, \diamond ; 57 cm, \circ .

layer generated by the impermeable wall increases rapidly. Figures 21 and 22 describe the evolutions of the dimensionless turbulent stresses normalized by the bulk velocity $\langle \tau_{ii} \rangle^{1/2} / u_m$ ($i=1,3$) in the streamwise and normal directions with available experimental data. As a result of simulation, it is found that the flow turbulence intensity in each section of the channel is reasonably predicted. However, some minor discrepancies remain in regard to the stress profiles in the vicinity of the two walls. The simulation reveals the presence of turbulent peaks in the wall regions, whereas the present experimental data describe quasiflate evolutions for each section. This disagreement is mainly attributed to the measurements which are altered in the vicinity of the walls. Indeed, the probe (diameter $150 \mu\text{m}$) is introduced from the impermeable wall along the normal direction x_3 in the channel height (1.03 cm). Because of the probe dimension which is not negligible to the channel height, the flow is locally perturbed. In that condition, the probe is assumed to provide averaged measurements on the wire length integration. This is obviously the case for the impermeable wall region where the turbulent peak occurs in the buffer layer (see Fig. 8) and is not captured by the present experiment. For the fully turbulent flow regime, note that the lowest cutoff frequency given by the cutoff wave number is $\nu_c = \kappa_c u_m / 2\pi \approx 100 \text{ kHz}$, whereas the typical upper frequency of the probe is about 20 kHz, so that the probe filters the high frequencies of the signal. Having in mind the previous discussion, we are led to think that the turbulence intensity obtained by the LES and compared to the experiment (particularly for the stresses) plotted in Figs. 20–22 is in fact reasonably predicted. These

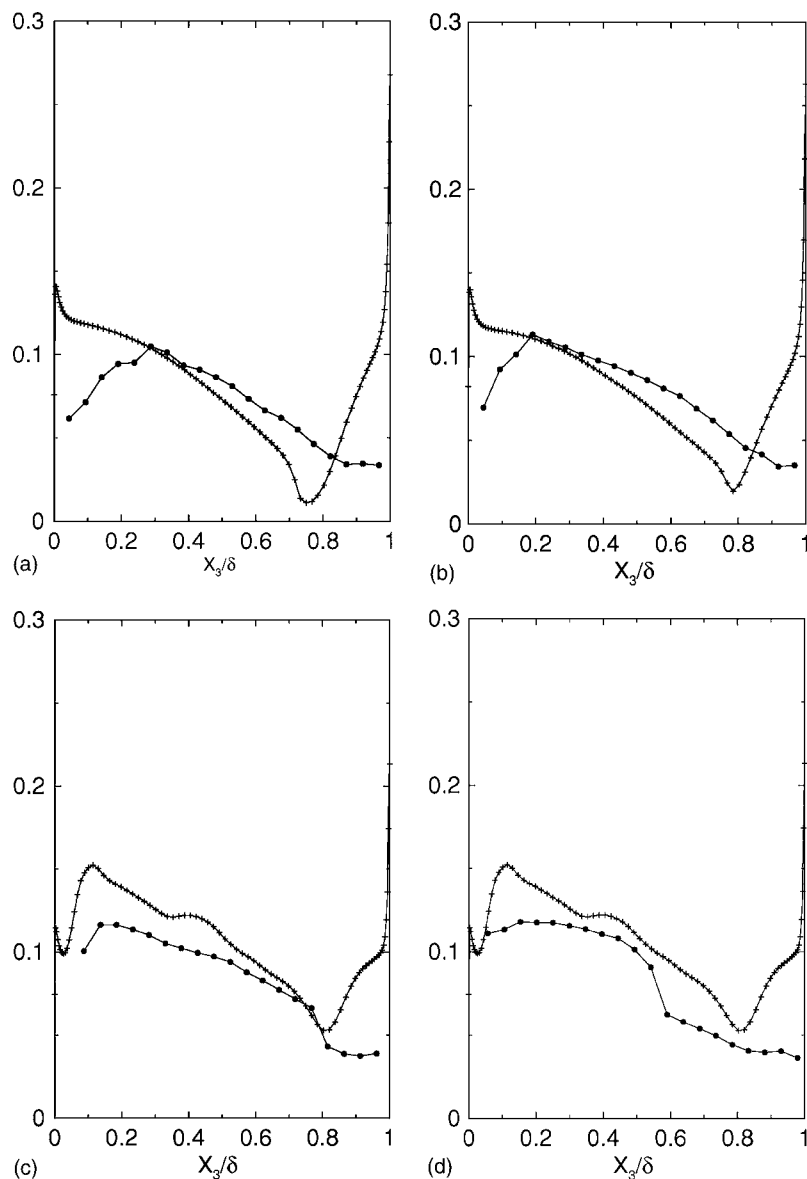


FIG. 21. Streamwise turbulent stresses. +, $\langle(\tau_{11})^{1/2}\rangle/u_m$; ●, experimental data; (a) $x_1=40$ cm; (b) 45 cm; (c) 50 cm; (d) 57 cm.

figures reveal also other flow characteristics. It can be seen that the turbulence is more developed in the permeable wall region than for the impermeable wall region, so that the feature of the fluid injection is to shift the turbulence toward the core flow. Figure 23 shows the evolutions of the shear stress $\langle\tau_{13}\rangle/u_m^2$ at different cross sections in the channel. A good agreement is obtained with the experimental data. In comparison with the standard distribution of wall-bounded flows, the fluid injection through the surface yields nonsymmetry shear stress profiles. In order to characterize the part of the modeled turbulent scales among the part of the resolved scales, the LES and SGS stresses $\langle\tau_{33}\rangle^{1/2}$ are plotted in the last section $x_1=57$ cm when the flow is fully turbulent, as shown by Fig. 24. One can observe that the intensity of the large-scale part remains greater than those of the subgrid-scale part, particularly in the core flow. It is also noticed in Fig. 24 that the large-scale part follows very well the measurements of the probe which is not sensitive to high frequencies as mentioned previously.

VII. CONCLUSION

A new partially integrated transport model for subgrid-scale stresses and dissipation rate has been proposed for LES of unsteady flows which present nonequilibrium turbulence spectra. As a result of modeling in the spectral space, a formally continuous derivation of the model has been obtained when the cutoff location is varied, which guaranties compatibility with the two extreme limits that are the full statistical Reynolds stress model and direct numerical simulation. The present model has been successfully calibrated on the well-known fully turbulent channel flow. The application to the channel flow with wall injection then has been considered for illustrating the potentials of the method. It has been found that the different flow regimes as well as the transition phenomena are well reproduced and that the velocities and the turbulent stresses agree fairly well with the experimental data. Moreover, the flow structures have been analyzed in detail. More extensive applications should be, however, nec-

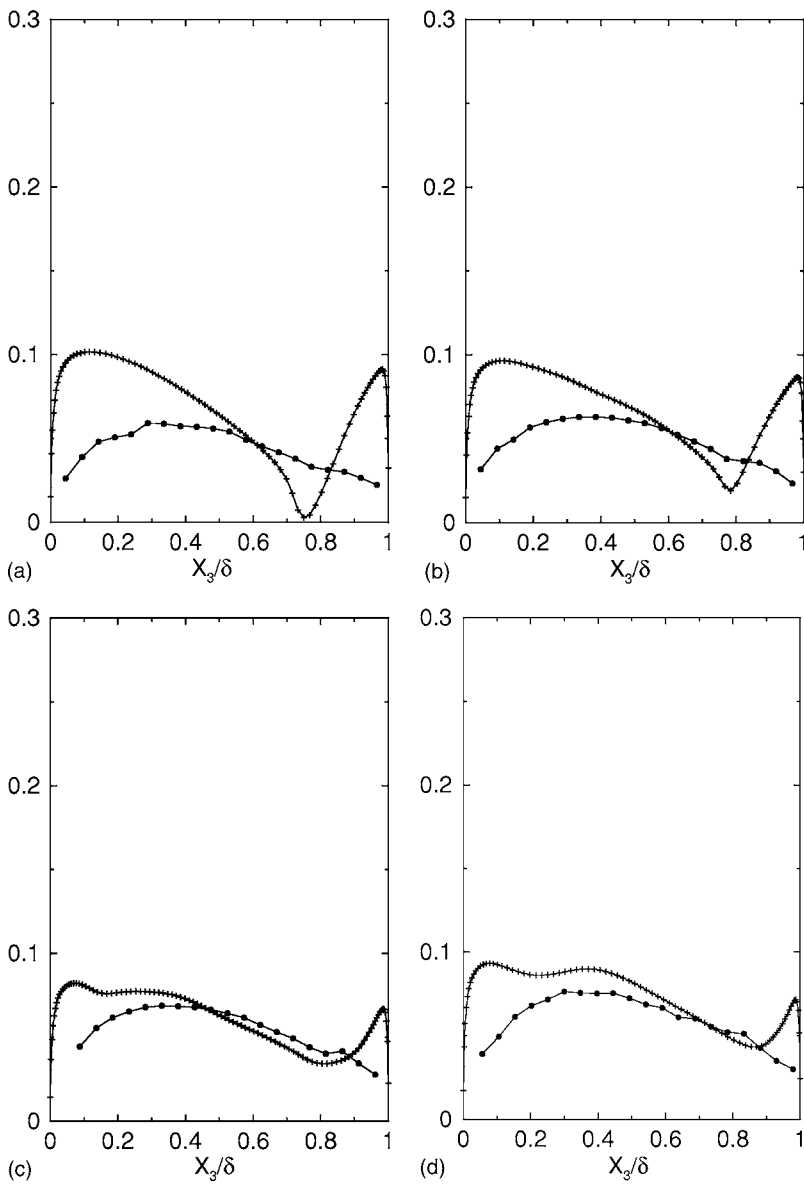


FIG. 22. Normal turbulent stresses. +, $\langle(\tau_{33})^{1/2}\rangle/u_m$; ●, experimental data; $x_1=40$ cm; 45 cm; 50 cm; 57 cm.

essary in the future to assess more thoroughly the proposed approach.

APPENDIX: EXACT TRANSPORT EQUATION OF THE TURBULENT SUBGRID-SCALE ENERGY

Turbulent fluid with constant density is considered. The instantaneous Navier–Stokes equation for velocity is

$$\frac{\partial u_i}{\partial t} + \frac{\partial}{\partial x_j}(u_i u_j) = -\frac{1}{\rho} \frac{\partial p}{\partial x_i} + \nu \frac{\partial^2 u_i}{\partial x_j \partial x_j}. \tag{A1}$$

In a first approximation, disregarding the higher order terms, the filtered equation can be written as

$$\frac{\partial \bar{u}_i}{\partial t} + \frac{\partial}{\partial x_j}(\bar{u}_i \bar{u}_j) = -\frac{1}{\rho} \frac{\partial \bar{p}}{\partial x_i} - \frac{\partial}{\partial x_j} \overline{u_i' u_j'} + \nu \frac{\partial^2 \bar{u}_i}{\partial x_j \partial x_j}. \tag{A2}$$

A term by term difference between these two equations

yields the transport equation of the subgrid-scale fluctuating velocity:

$$\begin{aligned} \frac{\partial u_i'}{\partial t} + \bar{u}_j \frac{\partial u_i'}{\partial x_j} = & -u_j' \frac{\partial \bar{u}_i}{\partial x_j} - \frac{1}{\rho} \frac{\partial p'}{\partial x_i} + \frac{\partial}{\partial x_j} (\overline{u_i' u_j'} - u_i' u_j') \\ & + \nu \frac{\partial^2 u_i'}{\partial x_j \partial x_j}. \end{aligned} \tag{A3}$$

The instantaneous velocity is then decomposed into the mean statistical velocity denoted $\langle u \rangle$, the large-scale velocity $v = \bar{u} - \langle u \rangle$, and the subgrid-scale fluctuation, so that the three term decomposition can be written as

$$u = \langle u \rangle + v + u'. \tag{A4}$$

Taking into account this decomposition, Eq. (A3) is rewritten as follows:

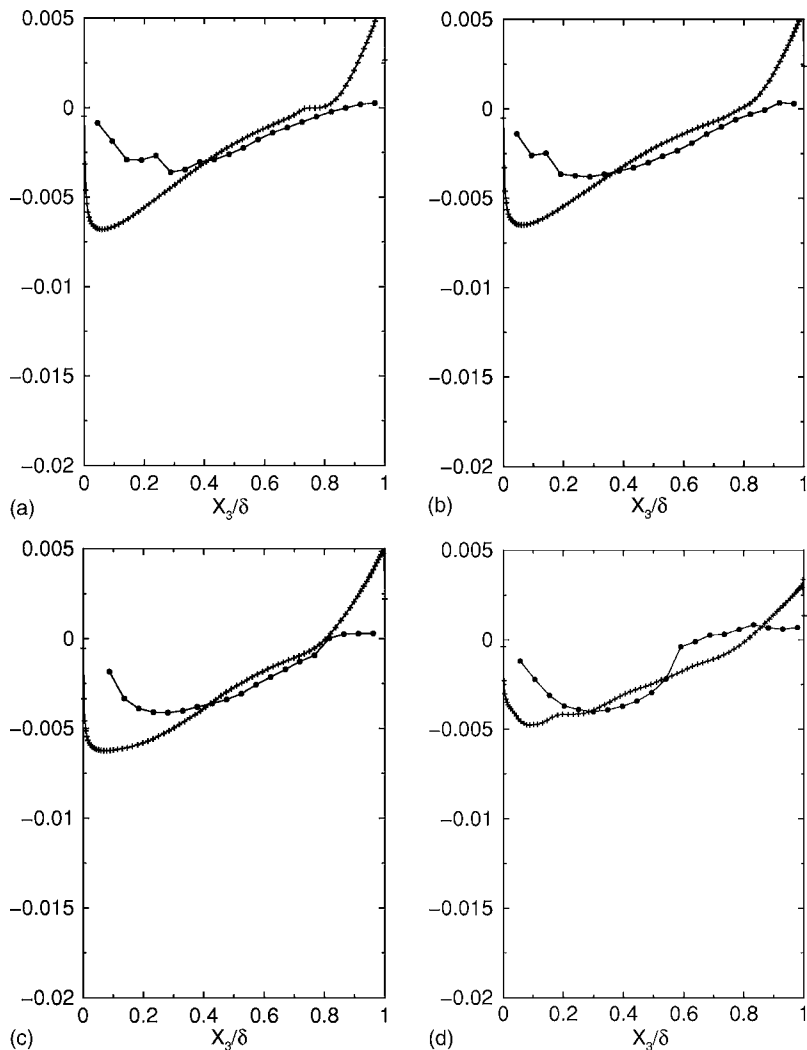


FIG. 23. Shear stresses. +, $\langle \tau_{13} \rangle / u_m^2$; ●, experimental data; (a) $x_1=40$ cm; (b) 45 cm; (c) 50 cm; (d) 57 cm.

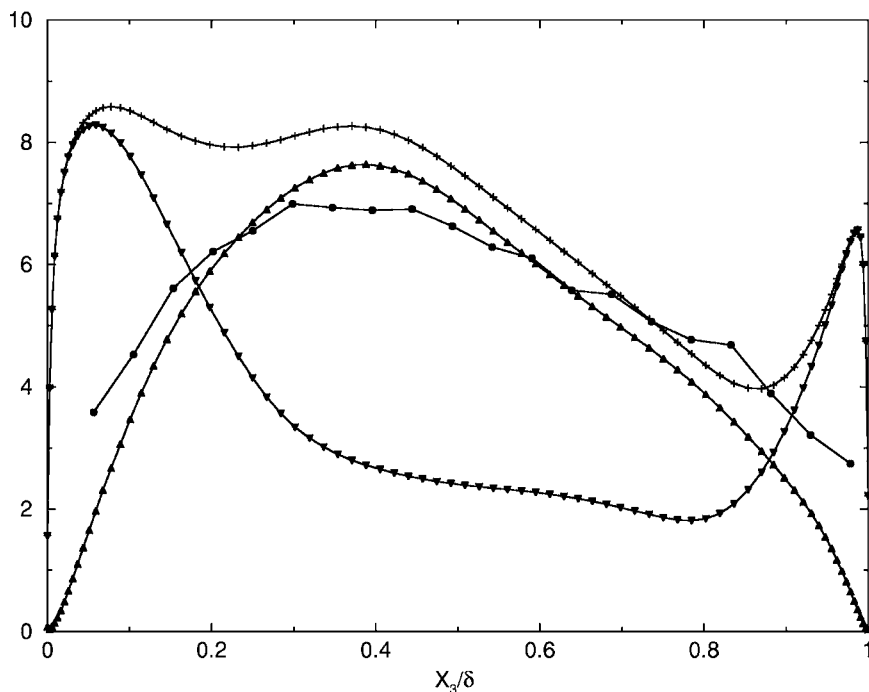


FIG. 24. Normal turbulent stresses (m/s). ▼, $\langle (\tau_{33})_{SGS} \rangle^{1/2}$; ▲, $\langle (\tau_{33})_{LES} \rangle^{1/2}$; +, $[\langle (\tau_{33})_{SGS} \rangle + \langle (\tau_{33})_{LES} \rangle]^{1/2}$; ●, experimental data; $x_1=57$ cm.

$$\begin{aligned} \frac{\partial u_i'}{\partial t} + \langle u_j \rangle \frac{\partial u_i'}{\partial x_j} = & -u_j' \frac{\partial \langle u_i \rangle}{\partial x_j} - \frac{1}{\rho} \frac{\partial p'}{\partial x_i} + \frac{\partial}{\partial x_j} \overline{(u_i' u_j' - u_i' u_j')} \\ & - u_j' \frac{\partial v_i}{\partial x_j} - v_j \frac{\partial u_i'}{\partial x_j} + \nu \frac{\partial^2 u_i'}{\partial x_j \partial x_j}. \end{aligned} \quad (\text{A5})$$

Equation (A5) is multiplied by the fluctuating velocity u_i' . By applying the statistical averaging to this equation, the transport equation of the subgrid-scale turbulent kinetic energy $k_{SGS} = \langle u_i' u_i' \rangle / 2$ is obtained which then reads

$$\begin{aligned} \frac{\partial k_{SGS}}{\partial t} + \langle u_j \rangle \frac{\partial k_{SGS}}{\partial x_j} = & -\langle u_i' u_j' \rangle \frac{\partial \langle u_i \rangle}{\partial x_j} - \left\langle u_i' u_j' \frac{\partial v_i}{\partial x_j} \right. \\ & - \nu \left\langle \frac{\partial u_i'}{\partial x_j} \frac{\partial u_i'}{\partial x_j} \right\rangle - \frac{1}{2} \frac{\partial}{\partial x_j} \langle u_i' u_i' (u_j' \\ & + v_j) \rangle - \frac{1}{\rho} \frac{\partial}{\partial x_i} \langle u_i' p' \rangle + \nu \frac{\partial^2 k_{SGS}}{\partial x_j \partial x_j}. \end{aligned} \quad (\text{A6})$$

Interpretation of the different terms in the right-hand side of Eq. (A6) is given in the following. The first term represents the turbulence production caused by the mean and large-scale velocity gradients, the second term corresponds to the transfer process due to the action of large-scale structures on the subgrid-scale turbulence, the third term is the viscous dissipation rate and the other terms are related to the turbulent and viscous diffusion processes. Equation (A6) is equivalent to Eq. (23) in which the terms decomposition (A4) is introduced.

- ¹C. G. Speziale, S. Sarkar, and T. B. Gatski, "Modelling the pressure-strain correlation of turbulence: An invariant dynamical systems approach," *J. Fluid Mech.* **227**, 245 (1991).
- ²B. Chaouat, "Simulations of channel flows with effects of spanwise rotation or wall injection using a Reynolds stress model," *ASME J. Fluids Eng.* **123**, 2 (2001).
- ³B. Chaouat, "Numerical predictions of channel flows with fluid injection using Reynolds stress model," *J. Propul. Power* **18**, 295 (2002).
- ⁴J. Smagorinsky, "General circulation experiments with the primitive equations," *Mon. Weather Rev.* **91**, 99 (1963).
- ⁵J. Deardorff, "A numerical study of three-dimensional turbulent channel flow at large Reynolds number," *J. Fluid Mech.* **41**, 433 (1970).
- ⁶P. Moin and J. Kim, "Numerical investigation of turbulent channel flow," *J. Fluid Mech.* **118**, 341 (1982).
- ⁷M. Lesieur and O. Métais, "New trends in large-eddy simulations of turbulence," *Annu. Rev. Fluid Mech.* **28**, 45 (1996).
- ⁸M. Germano, U. Piomelli, P. Moin, and W. H. Cabot, "A dynamic subgrid-scale eddy-viscosity model," *Phys. Fluids A* **3**, 1760 (1991).
- ⁹O. Métais and M. Lesieur, "Spectral large-eddy simulation of isotropic and stably stratified turbulence," *J. Fluid Mech.* **239**, 157 (1992).
- ¹⁰U. Schumann, "Subgrid scale model for finite difference simulation of turbulent flows in a plane channel annuli," *J. Comput. Phys.* **18**, 367 (1975).
- ¹¹K. Horiuti and A. Yoshizawa, "Large-eddy simulation of turbulent flow by 1-equation model," in *Notes on Numerical Fluid Mechanics, Direct and Large Eddy Simulations of Turbulence*, edited by U. Schumann and R. Friedrich (Vieweg, 1986), Vol. 15, pp. 119.
- ¹²A. Dejoan and R. Schiestel, "LES of unsteady turbulence via a one-equation subgrid-scale transport model," *Int. J. Heat Fluid Flow* **23**, 398 (2002).
- ¹³J. W. Deardorff, "The use of subgrid transport equations in a three-

- dimensional model of atmospheric turbulence," *ASME J. Fluids Eng.* **95**, 429 (1973).
- ¹⁴A. Dejoan and R. Schiestel, "Large eddy simulations of non-equilibrium pulsed turbulent flows using transport equation subgrid model," *Proceeding of the Second Symposium on Turbulent Shear Flow Phenomena*, edited by E. Lindborg, A. Johansson, J. Eaton, J. Humphrey, N. Kasagi, M. Leschziner, and M. Sommerfeld (University of Stockholm, 2001), Vol. 2, pp. 341–346.
- ¹⁵R. Schiestel and A. Dejoan, "Towards a new partially integrated transport model for coarse grid and unsteady turbulent flow simulations," *Theor. Comput. Fluid Dyn.* **18**, 443 (2005).
- ¹⁶B. E. Launder and N. Shima, "Second moment closure for the near wall sublayer: Development and application," *AIAA J.* **27**, 1319 (1989).
- ¹⁷M. Germano, "From RANS to DNS: Toward a bridging model," in *Direct and Large-Eddy Simulation III, ERCOFTAC Series*, edited by P. Voke, N. D. Sandham, and L. Kleiser (Kluwer Academic, Dordrecht, 1999), Vol. 7, pp. 225–236.
- ¹⁸P. R. Spalart, "Strategies for turbulence modelling and simulations," *Int. J. Heat Fluid Flow* **21**, 252 (2000).
- ¹⁹R. Moser, D. Kim, and N. Mansour, "Direct numerical simulation of turbulent channel flow up to $Re_\tau=590$," *Phys. Fluids* **11**, 943 (1999).
- ²⁰B. Chaouat and R. Schiestel, "Reynolds stress transport modelling for steady and unsteady channel flows with wall injection," *J. Turbul.* **3**, 1 (2002).
- ²¹B. Wasistho and R. D. Moser, "Simulation strategy of turbulent internal flow in solid rocket motor," *J. Propul. Power* **21**, 251 (2005).
- ²²A. Favre, "Equations des gaz," *J. Mec.* **4**, 362 (1963).
- ²³R. Schiestel, "Sur le concept d'échelles multiples en modélisation des écoulements turbulents. part II," *J. Mec. Theor. Appl.* **2**, 601 (1983).
- ²⁴M. M. Gibson and B. E. Launder, "Ground effects on pressure fluctuations in the atmospheric boundary layer," *J. Fluid Mech.* **86**, 491 (1978).
- ²⁵R. Schiestel, "Multiple-time-scale modeling of turbulent flows in one-point closures," *Phys. Fluids* **30**, 722 (1987).
- ²⁶R. Schiestel, "Sur le concept d'échelles multiples en modélisation des écoulements turbulents. part I," *J. Mec. Theor. Appl.* **2**, 417 (1983).
- ²⁷J. O. Hinze, *Turbulence* (McGraw-Hill, New York, 1975).
- ²⁸M. Lesieur, *Turbulence in Fluid*, 2nd ed. (Kluwer Academic, Dordrecht, 1990).
- ²⁹U. Schumann, "Realizability of Reynolds stress turbulence models," *Phys. Fluids* **20**, 721 (1977).
- ³⁰C. G. Speziale, R. Abid, and P. A. Durbin, "On the realizability of Reynolds stress turbulence closures," *J. Sci. Comput.* **9**, 369 (1994).
- ³¹B. Chaouat, "Numerical simulations of fully developed channel flows using $k-\epsilon$, algebraic and Reynolds stress models," *AIAA Paper No. 99-0158* (1999).
- ³²Ph. Roy, "Résolution des équations de Navier–Stokes par un schéma de haute précision en espace et en temps," *Rech. Aerosp.* **6**, 373 (1980).
- ³³J. L. Lumley, "Computational modeling of turbulent flows," *Adv. Appl. Mech.* **18**, 123 (1978).
- ³⁴C. R. Smith and S. P. Lesieur, "The characteristics of low-speed streaks in the near-wall region of a turbulent boundary layer," *J. Fluid Mech.* **129**, 27 (1983).
- ³⁵J. Kim, P. Moin, and R. Moser, "Turbulence statistics in fully developed channel flow at low Reynolds number," *J. Fluid Mech.* **177**, 133 (1987).
- ³⁶B. Chaouat, "Flow analysis of a solid propellant rocket motor with aft fins," *J. Propul. Power* **13**, 194 (1997).
- ³⁷A. Gany and I. Aharon, "Internal ballistics considerations of nozzleless rocket motors," *J. Propul. Power* **15**, 866 (1999).
- ³⁸J. S. Sabnis, R. K. Madabhushi, H. J. Gibeling, and H. McDonald, "On the use of $k-\epsilon$ turbulence model for computation of solid rocket internal flows," *AIAA Paper No. 89-2558* (1989).
- ³⁹R. A. Beddini, "Injection-induced flows in porous-walled ducts," *AIAA J.* **11**, 1766 (1986).
- ⁴⁰U. Piomelli, P. Moin, and J. Ferziger, "Large eddy simulation of the flow in a transpired channel," *J. Thermophys. Heat Transfer* **5**, 124 (1991).
- ⁴¹S. A. Apte and V. Yang, "A large-eddy simulation study of transition and flow instability in a porous-walled chamber with mass injection," *J. Fluid Mech.* **477**, 215 (2003).
- ⁴²G. Avalon, G. Casalis, and J. Griffond, "Flow instabilities and acoustic resonance of channels with wall injection," *AIAA Paper No. 98-3218* (1998).